Nowaczyk, N. (2011): Dissolution of titanomagnetite and sulphidization in sediments from Lake Kinneret, Israel. - Geophysical Journal International, 187, 1, pp. 34—44.

DOI: http://doi.org/10.1111/j.1365-246X.2011.05120.x

Geophysical Journal International

Geophys. J. Int. (2011) **187,** 34–44 doi: 10.1111/j.1365-246X.2011.05120.x

Dissolution of titanomagnetite and sulphidization in sediments from Lake Kinneret, Israel

Norbert R. Nowaczyk

Helmholtz Centre Potsdam, GFZ German Centre for Geoscience, Section 5.2—Climate Dynamics and Landscape Evolution, Telegrafenberg, D-14473 Potsdam, Germany. E-mail: nowa@gfz-potsdam.de

Accepted 2011 June 21. Received 2011 June 20; in original form 2010 October 8

SUMMARY

Magnetic extracts obtained from sediment cores recovered from Lake Kinneret, Israel, were subjected to comprehensive scanning electron microscope and in-line energy dispersive X-ray spectroscopy analyses. A variety of ferrimagnetic iron oxides and iron sulphide particles were identified, along with apparently non-magnetic iron sulphides. The majority of the iron oxides are titanomagnetites that have undergone pervasive dissolution, and in many cases were only preserved as skeletal, 3-D lattices of ilmenite lamellae. Often the spaces between the submicron ilmenite lamellae are empty. Also sponge-like dissolution features are observed in some residual titanomagnetite grains. Another group of titanomagnetite grains is characterized by superficial shrinkage-cracks, which indicate low-temperature maghemitization. In some cases, these cracks appear to be where dissolution started. Most titanomagnetites contain impurities of Al, Mg, Si and Mn on the order of 1 per cent. Chromium-magnetites, with minor Ti, Mg and Al content on the order of a few percent, but without Mn, were also found. Chromium-magnetites mostly occur as octahedra in a well-preserved state, which indicates that they are less prone to dissolution. Magnetite spherules of 40–60 μm in size, which were mostly hollow, were only found in material collected from the outer zone of the core section that was in contact with the steel core barrel. These spherules were not found in material collected from the centre of the core. They are therefore interpreted as contaminants that were produced during fabrication of the steel core barrel. Iron sulphides are present as pyrite, either as larger aggregates of cubic crystals, each of up to 20 μm in size, or as 5–10 μm framboidal aggregates, consisting mostly about 0.3 μm idiomorphic octahedra. The cubic pyrite crystals have heterogeneous compositions. Pure pyrite should be non-magnetic, but even aggregates of up to 150 μm in size were magnetically separated. They probably therefore contain a magnetic core of greigite or overgrown titanomagnetite. The latter possibility is supported by observations of residual titanomagnetites with individual pyrite crystals residing directly on their surfaces, or filling space between ilmenite lamellae. Irregular aggregates of flaky, submicron iron sulphides were also found, which are interpreted to be greigite. The greigite has a low degree of visible crystallization. Pyrite and/or greigite grains were found inside the aggregates, or in agglomerates with organic remnants. Together, visual observations and elemental analyses provide clear evidence of pervasive dissolution of primary titanomagnetite and concurrent sulphidization of sediments from Lake Kinneret.

Key words: Magnetic mineralogy and petrology; Magnetostratigraphy; Rock and mineral magnetism.

INTRODUCTION

Magnetite dissolution is ubiquitous in suboxic and anoxic environments (e.g. Karlin & Levi 1983; Canfield & Berner 1987; Karlin *et al.* 1987; Channell & Hawthorne 1990, Karlin 1990a,b; Leslie *et al.* 1990a,b). A classical example from the marine realm is the recurring formation of sapropels in the eastern Mediterranean Sea triggered by insolation variations (e.g. Dekkers *et al.* 1994; Larrasoaña *et al.* 2003). Sapropel formation is accompanied by complex non-steady-state diagenetic dissolution and precipitation patterns of iron oxides and iron sulphides, respectively. A similar scenario was derived from Lake El'gygytgyn, NE Siberia (Nowaczyk *et al.* 2002, 2007). By combining rock magnetic data with biogenic silica (opal), total organic carbon (TOC), total sulphur (TS) and elemental

data, it could be shown that recurring anoxic conditions at the lake floor, mostly triggered by the Earth's precession cycles, caused dissolution of 90 to 99 per cent of the magnetic fraction during these time intervals (Nowaczyk *et al*. 2002, 2007). The dissolved iron has been subsequently incorporated into secondary vivianite nodules (Minyuk *et al.* 2007). In a comprehensive study of three parallel cores from Lake Kinneret, Israel, it was inferred from rock magnetic and X-ray diffraction (XRD) analyses that the primary iron oxide magnetic fraction was partly dissolved and was subsequently replaced by the magnetic iron sulphide greigite [see the recent review on sedimentary greigite by Roberts *et al.* (2011)] and by non-magnetic iron sulphides. However, as is the case in several other studies, the loss of detrital magnetic carrier minerals has been inferred indirectly (e.g. Karlin 1990a,b; Leslie *et al.* 1990a,b; Nowaczyk *et al.* 2000, 2002). The intention of this study is to directly visualize evidence for severe titanomagnetite dissolution and/or etching in sediments from Lake Kinneret, and to illustrate the formation of iron sulphides using scanning electron microscope (SEM) images, such as has been done by, for example, Canfield & Berner (1987), Channell & Hawthorne (1990), Rowan & Roberts (2006), Rowan *et al.* (2009), and accompanying energy dispersive X-ray spectroscopy (EDS).

MATERIAL AND METHODS

Geological setting and coring procedure

Lake Kinneret is sited in the depression of the Dead Sea—Jordan Rift valley in northern Israel (32° 49′ N, 35° 36′E). Currently, this freshwater lake is 43 m deep and its surface lies at around 208 m b.s.l. (below sea level). Lake level varies by metres, depending on precipitation and temperature. The modern catchment area of Lake Kinneret (dashed lines in Fig. 1) is dominated by Tertiary to Quaternary volcanics, mainly basalts and basanites, which are important possible sources of magnetic particles to the lake. However, it is important to note that, during the last glacial maximum at around 26–24 kyr BP, Lake Kinneret and the Dead Sea merged into a single water body named Lake Lisan, with its water level at around 175 m b.s.l. (Bartov *et al.* 2002; Hazan *et al.* 2005). Thus, the catchment extended significantly to the south during the last glacial. Approaching the termination of the last glacial, water level dropped again, which separated Lake Lisan into freshwater Lake Kinneret and the hypersaline Dead Sea terminal lake, respectively.

In 1999, several sediment cores were taken with Usinger type piston corers at the southwestern shore of Lake Kinneret during a lake level low stand at the archaeological site Ohalo (Ron *et al.* 2007) which was flooded again some years later. The deployed piston corer has core barrels (diameter 80 mm) made from 1-mm-thin steel tubes and does not contain plastic liners. Thus, the sediments are extruded from the core barrels in the laboratory. During extrusion, a thin nylon fibre was used to split the sediment column into two halves, which were simultaneously pushed into two half plastic tubes as working and archive halves. For storage at 4 °C, split cores were sealed in plastic sleeves. The recovered sediments are either laminated or massive. Laminae are composed of clay and silt, alternating with calcite. The massive sediments contain variable mixtures of silt and clay.

For this study, sediments from depths of 110–160 cm from the 460 cm core KIN5A (Fig. 2) were chosen for detailed analyses of the magnetic remanence carriers. Magnetic extraction and SEM analyses were used here because the presence of both magnetite and greigite were revealed from rock magnetic and XRD analyses (Ron *et al.* 2007). The age of the archaeological site Ohalo is about 20 ka. This is taken as the age of the top of core KIN5A. A single AMS (accelerator mass spectrometry) ^{14}C age obtained from a coal chunk found at a depth of 260 cm in core KIN5A yielded an age of 33 ka (Ron *et al.* 2007). The depth interval between 110 and 160 cm therefore has an age of about 26–30 ka. However, an age of only 21.4 ka was obtained from parallel core KIN2A (just 4 m apart) for a 'Melanopsis' sample (fresh water gastropod) from a depth of 230 cm. Therefore, the age of the investigated sediments could be younger than 26–30 ka, but not younger than 20 ka.

Preparation of magnetic extracts

A comprehensive overview of methods for extracting magnetic particles from sediments is given by Hounslow & Maher (1999). However, it was clear from Ron *et al.* (2007) that magnetite dissolution must have occurred in Lake Kinneret, therefore, a simple technique for extracting magnetic particles was applied. To prepare magnetic extracts, about 2–4 cm^3 of sediment was used. A first set of samples was taken from four intervals along the outer zone of the working half of the core (Fig. 2), whereas a second set of five samples was collected from palaeomagnetic samples (6 cm^3 plastic boxes) that were previously taken along the central axis of the split core. Both sets of samples were taken from about the same stratigraphic level in core KIN5A (Fig. 2). Each sediment sample was dispersed into about 50 cm^3 of alcohol using ultrasound, and each resulting slurry was whirled for 5–10 min. Extraction of magnetic minerals was performed with two different probes (Fig. 3) submersed repeatedly into the slurry, with and without ultrasound action. The type A consists of strong rare earth magnets (diameter 20 mm) sitting on top of a flux-focussing iron finger (diameter 4 mm). The iron finger was placed into a thin-walled plastic hose and magnetic particles were attracted to the hose around the tip of the iron needle. The type B probe consists of a large, partly conical plastic hose which takes up the whole magnet and iron finger assemblage of probe Type A, but upside-down. Thus, the whole magnet can be submerged into the slurry, with the much larger magnetic flux providing a much larger area for collecting magnetic particles. In Type B probes, the iron finger is used to remove the magnet from the plastic hose. These probes are efficient for collecting large amounts of magnetic particles in a short time. Each time, after switching off the ultrasound, the extraction probes were moved gently through the slurry for about a minute, then taken out, and finally magnetic material was carefully cleared with drops of alcohol. The magnetic particles were collected from the plastic hose, after removing the iron finger (Type A) or magnet (Type B) from the corresponding plastic hose, by flushing them carefully into small vials with alcohol. Alcohol was used instead of water to avoid oxidation of magnetic minerals, especially iron sulphides like greigite, during extraction and subsequent storage of the particles. Another advantage of alcohol is that it evaporates quickly to enable drying of the collected particles for investigation.

Particle imaging and elemental analyses

A Carl Zeiss SMT Ultra 55 Plus SEM with various electron detectors and integrated EDS facility was used for analyses. The SEM has a spatial resolution of 1 nm at 15 keV. Some older analyses were performed with a Zeiss DSM 962 SEM. In general the incident electron beam causes several effects at and within the surface of the

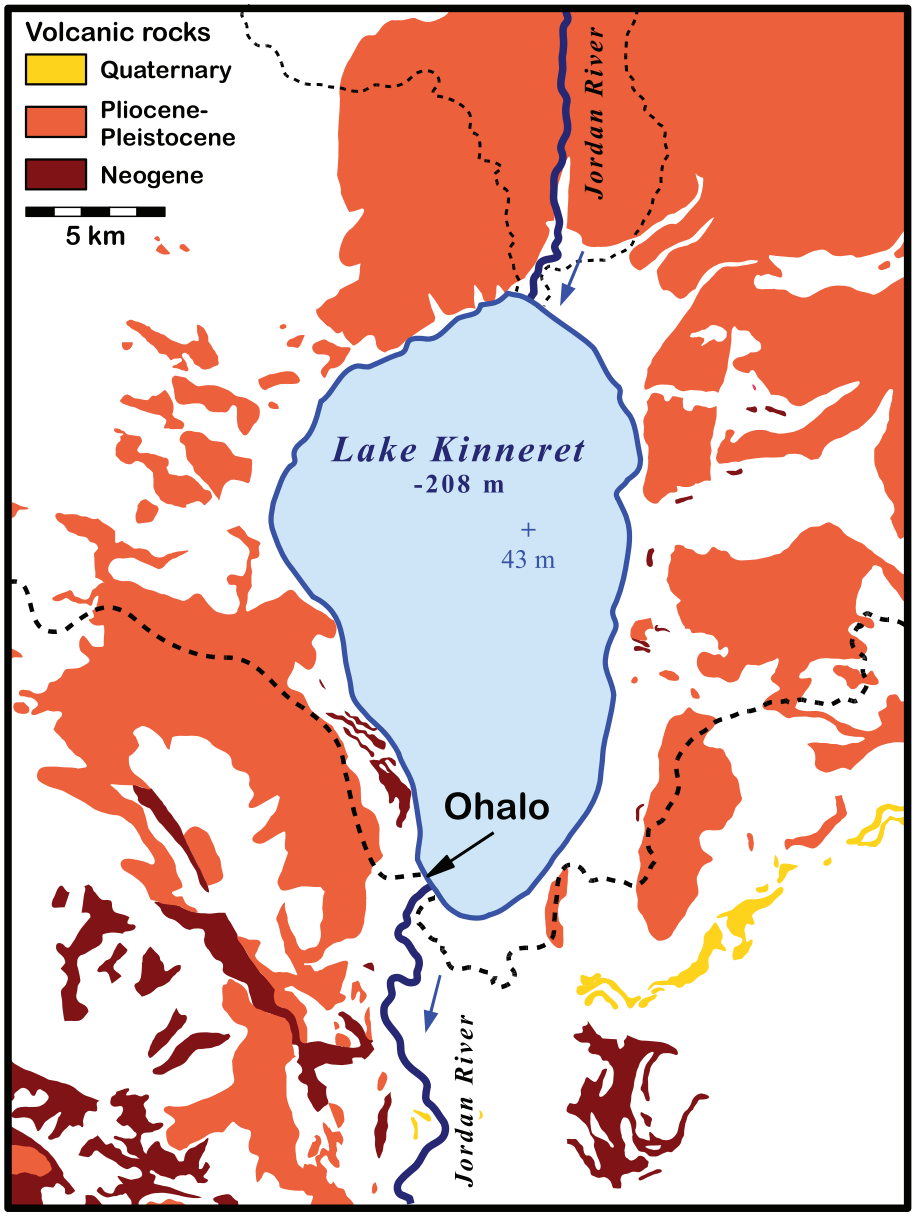

Figure 1. Simplified geological map of the Lake Kinneret area, northern Israel (redrawn from a map provided by the Geological Survey of Israel): distribution of Tertiary and Quaternary volcanic rocks, basalts and basanites around the lake as important sources of detrital magnetic particles. The studied core was recovered from archaeological site Ohalo on the southwestern shore during a lake level low stand (temporarily underwater afterward). The catchment for Lake Kinneret is marked by thick dashed lines, whereas thin dashed lines mark the drainage area of the upper Jordan River, which enters Lake Kinneret in the north.

target under analysis. Emission of secondary as well as backscattered electrons can be used for imaging. The energy spectrum of emitted X-rays is unique for every element, with the energy of the spectral lines moving to higher values with increasing atomic number. The intensity of backscattered electrons is proportional to the atomic number of the elements in an analysed particle. Therefore, backscattered electron imaging gives immediately valuable information about compositional differences among mineral grains. Iron oxides and sulphides with relatively heavy ions (O = 8, S = 16, Ti = 22, Cr = 24, Mn = 25 and Fe = 26) appear much brighter than silicates (O = 8, Na = 11, Mg = 12, Al = 13 and Si = 14) and carbonates (C = 6, O = 8 and Ca = 20) which are composed mainly of relatively light elements. Only barite, which is a common mineral in anoxic sediments (O = 8, S = 16 and Ba = 56) appears brighter than magnetic minerals. Detrital magnetic particles are not necessarily different in shape from non-magnetic detrital particles, therefore the backscatter mode was preferred for identifying remanence carriers within the magnetic extracts.

Magnetic extracts were fixed onto standard SEM stubs using double-sided sticky tape. One additional parallel sample (from 140.9 to 142.9 cm) was prepared as a polished section by embedding the extracted particles into epoxy. This enabled the analysis especially of the interior of certain extracted particles. For SEM imaging, objects must be sputtered with a conducting material. Sample set KIN5A-1 to KIN5A-4 was sputtered with a gold/palladium (Au/Pd) alloy. This yields better images, but elemental analyses are hampered by strong X-ray spikes from Au in the 2.2 keV energy range, where lighter elements have their main (Kα, Kβ, Lα and Lβ) X-ray

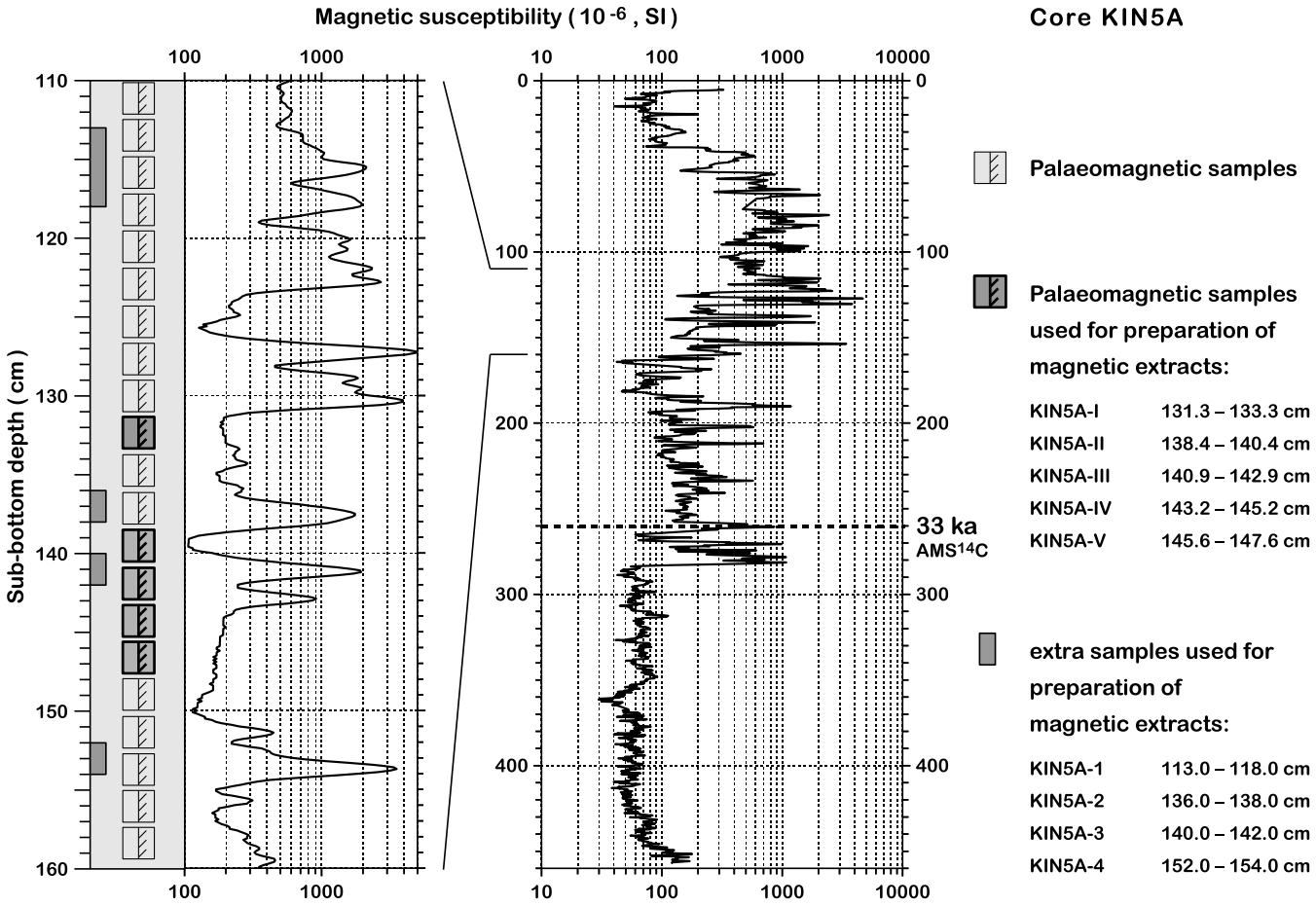

Figure 2. Downcore variations of magnetic susceptibility in core KIN5A. The sampling scheme for palaeomagnetic samples as well as for extra samples are shown on the left-hand schematic. The exact depth values for samples used for magnetic extraction are listed on the right.

emissions. Sample set KIN5A-I to KIN5A-V was prepared mainly for elemental analyses. Therefore, these samples were covered with carbon (Kα at 0.282 keV), which only causes limitations at high magnifications.

In the EDS elemental analyses the height of the elemental spikes is also geometrically influenced. Analyses from inclined crystal planes can be different from those from planes oriented perpendicular to the analysing beam. Therefore, most particles were analysed at several points, sometimes even along lines consisting of 40–50 individual analyses.

For faster analyses, most of the SEM work was performed with a target distance of 12–13 mm and an aperture of 120 μm, which is the best for elemental analyses in the instrument used. Useful images could also be taken with these settings at magnifications of up to $\times$4000 in the backscatter (BSc) mode. Nevertheless, imaging yielded best results with a target distance of only 5–6 mm and an aperture of 30 μm, especially with the Inlens (InL) detector and the secondary electron (SE) detector, respectively.

RESULTS

Some 340 images (including 140 EDS reference images), 550 point analyses and 16 line scans, each consisting of 40 or 50 spot readings, were obtained. Many magnetic minerals and (apparently) non-magnetic particles were identified in nine studied extracts from Lake Kinneret sediments. Representative results are shown in Plates 1–11. Identified magnetic minerals can be divided into two groups, iron oxides and iron sulphides. The iron oxides can be subdivided into detrital titanomagnetites, titanomaghemites, skeletal ilmenites, chromium-magnetites and pure magnetite spherules. The iron sulphides can be subdivided into non-magnetic pyrite which occur as either cubical crystals, or framboidal aggregates, and flaky, submicron magnetic particles, which are interpreted to be greigite, and which form ellipsoidal structures up to $\sim$10 μm across. Organic material, such as plant remains, pollen grains, algae and protozoa, which are mostly associated with magnetic iron sulphides, and some detrital silicate minerals were also identified. The presence of the latter can be explained partly by the simple extraction technique, in which a concentrated slurry and a simple cleaning procedure was used after extraction. The respective groups of (non-) magnetic particles are discussed in detail in the following subsections. EDS results are only shown for representative analyses.

Titanomagnetites, titanomaghemites and skeletal ilmenites

Detrital titanomagnetites extracted from core KIN5A have highly variable size, shape, composition and state of preservation (Plates 1–4). Only a few particles are more or less well preserved and idiomorphic in shape (Plates 1a and b). The octahedral, slightly skeletal crystals in Plate 1b are still attached to silicate rock matrix,

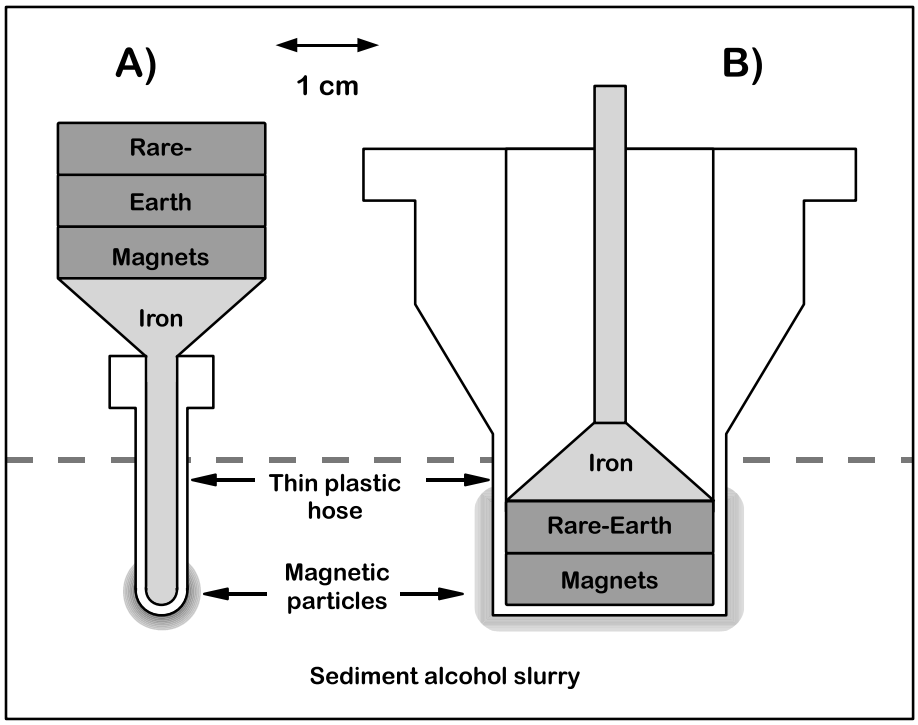

Figure 3. Sketch of the two extraction probes used for collecting magnetic particles. The rare earth magnets (dark grey) are attached to an iron finger (light grey) for flux focussing (Type A), and are protected by a plastic hose (white). Type B probes are similar to Type A probes, but the magnets and iron finger are turned upside-down, being completely protected by a large plastic hose (white). The dashed line indicates the surface of the slurry when the probes are submerged. The wall thickness of the protecting hoses submerged into the slurry is less than 0.5 mm.

as indicated in the EDS energy spectrum by Na, Al and Si peaks (Plate 1, lower left-hand diagram, yellow line). Several irregular particles are fragments of broken crystals and are well preserved (Plates 1c and d). The particle in Plate 1d, which was imaged with the backscatter sensor (BSc), has an apparent zoning in its upper plane. This should be due to compositional differences, but only a slightly higher oxygen peak is observed for the darker zones. Beside the zoning, this particle has a faint cross-hatched pattern of small cracks in its surface with an additional lamellar structure on its side. Other titanomagnetites have abundant shrinkage cracks (Plates 1e and f), which provide clear evidence for maghemitization. Maghemitization is commonly explained as the low-temperature ($T < 250\,^{\circ}$C) oxidation of (titano-) magnetite, but practically it is accomplished by migration of Fe ions out of the lattice which causes the observed shrinking effects and which strongly affects the magnetic properties of maghemite (Johnson & Merrill 1973; Petersen & Vali 1987; Cui *et al.* 1994; Zhou *et al.* 2001; Vahle *et al.* 2007; Gehring *et al.* 2009). EDS data for different spots on the grain fragment in Plate 1f contain similar peaks for Fe but significantly different Ti, O, Na, Al and Si peaks.

Traces of heavy etching are observable in the two titanomagnetite particles shown in Plate 2. The irregular fragment in Plates 2a–c has a dissected surface, which provides a view into its internal structure. The close-up views in Plates 2b and c indicate that large portions of this particle are porous arrangements of thin parallel-oriented layers with nothing between them. The other particle contains maghemitization features in the intact part of its surface but it is also fragmented at its edges. It appears that maghemitization cracks have opened the pathway for etching so that larger grain fragments could break off the lattice (Plates 2d–f).

Similar etching features that left sponge-like remnants separated by large cracks within titanomaghemite can be seen in Plates 3a–c. The particle appears to be brittle, with large portions already broken off. The etched titanomagnetite particle shown in Plates 3d and e has large cavities inside. The surface of the particle reflects action of etching acids, leaving a bark-like structure. Pitting corrosion features are evident in the particle shown in Plate 3f. This titanomagnetite also contains small contributions from Cr as well as Mg and Al, whereas other particles discussed earlier contain some Mn, Si or Mg. This is the only Cr-bearing titanomagnetite/maghemite particle with dissolution features found in the extracts. Chromium-magnetites form a group of remanence carriers of their own and therefore will be discussed separately later.

Plate 4 contains images of another large group of residual titanomagnetites. Although the grain in Plate 4a is a well-preserved, nearly idiomorphic octahedral titanomagnetite (shown for reference), the other crystals are only skeletons of ilmenite lamellae, oriented parallel to the octahedral [111] planes. In contrast to the example shown in Plate 4f, in many cases the space between the ilmenite lamellae, which originate from low-temperature exsolution of titanomagnetite, is empty. The thickness of the ilmenite lamellae is from 1.0 μm to 0.1 μm, which form brittle grids, such as shown in Plates 4d and f. The observation of preserved ilmenite while magnetite has been dissolved is consistent with investigations done and/or summarized by Canfield *et al.* (1992), which indicate that ilmenite, compared to magnetite, has a much lower reactivity in anoxic environments (table 4 and fig. 7 in Canfield *et al.* 1992). A similar, empirically derived conclusion was obtained by Roberts & Turner (1993) when analysing diagenetically reduced marine sediments from New Zealand. In numerous cases, the observed skeletal ilmenite grids in the Kinneret sediments are, in an ulcer-like manner, more or less overgrown by pyrite crystals, such as in Plates 4c, e and f. The Fe etched out of the titanomagnetites would have been

recycled directly into the iron sulphides (pyrite) that developed upon them. Similar pyrite overgrowths on iron oxides were observed by Canfield *et al.* (1992). Observations of iron sulphides are discussed later.

Chromium-magnetites

Another group of iron oxides, magnetites with a relatively high chromium content were identified in all analysed samples (Plate 5). The frequent large (up to 40 μm) chromium-magnetites are mostly idiomorphic octahedra (Plate 5b), sometimes with additional [110] planes (Plate 5b) or even with rounded edges (Plate 5d). Some of the chromium-magnetites are elongated along the [110] plane, such as the examples shown in Plates 5a, c and e. Dissolution features or superficial shrinkage cracks are rarely observed in chromium-magnetites, although some have a zoning or a lamella-like structure (Plates 5e and f). From the general appearance of all observed crystals it can be concluded that chromium-magnetites are less prone to early diagenetic dissolution than (titano-) magnetites, such as shown in Plates 1–4. A similar conclusion was drawn by, for example, Roberts & Turner (1993) and Hounslow (1996) for marine sediments that have undergone pervasive diagenetic dissolution of remanence carriers leaving, beside others, chromium-spinels.

Elemental analyses on Lake Kinneret chromium-magnetites yielded Ti:Cr:Fe (relative) weight-per cent ratios that range from 3:10:25 to 2:30:35, with further contributions by Mg and Al (ratio 1:2) of a few per cent. In contrast to the titanomagnetites, no Mn is present in the chromium-magnetites. The elemental compositions of the range of identified iron oxide minerals probably point to complex solid solution series in the host igneous rock of several minerals of the spinel group: magnetite (Fe_3O_4), ulvöspinel ($TiFe_2O_4$), chromite ($FeCr_2O_4$) and spinel ($MgAl_2O_4$). Literature about the magnetic properties of chromites and/or chromium-magnetite and magnetite containing other impurities different from Ti is sparse. After Francombe (1957) and Robbins *et al.* (1971), the Curie-temperature of chromium-magnetites ($FeCr_{2-x}Fe_xO_4$, with $0 \leq x \leq 2$), ranges (non-linearly) from about $-200\,^{\circ}$C for $x = 0$ (chromite) to 585 $^{\circ}$C for $x = 2$ (magnetite). Schmidtbauer (1983) discussed some magnetic properties of Fe-Cr-Ti spinels. A comprehensive discussion of the compositions of spinels from a wide variety of mafic to ultramafic igneous rocks is provided by Barnes & Roeder (2001). Chromium-magnetites can also occur in alkali-basalts, which are widely distributed around Lake Kinneret (Fig. 1). However, no detailed rock magnetic analyses are available from these rocks. According to Wasilewski *et al.* (1979) spinels from mantle xenoliths plot within a prism spanned by the six end-members (with composition and Curie-temperatures given in brackets): magnetite (Fe_3O_4, 585 $^{\circ}$C), magnesio-ferrite ($MgFe_2O_4$, 440 $^{\circ}$C), hercynite ($FeAl_2O_4$, -120 $^{\circ}$C), spinel ($MgAl_2O_4$, non-magnetic), chromite ($FeCr_2O_4$, -210 $^{\circ}$C) and magnesio-chromite ($MgCr_2O_4$, -257 $^{\circ}$C). They concluded that substitution of Cr, Mg and Al into magnetite all lower the Curie point, which is the reason why most mantle xenoliths have weak to negligible magnetizations (see also Richards *et al.* 1973). The Curie point is also lowered with increasing Ti content (recent summary by Lattard *et al.* 2006), and increasing (Si, Mg) content (Kontny *et al.* 2004), which was not taken into account by Wasilewski *et al.* (1979). Thus, the Curie-temperature of the identified chromium-magnetites (with additional Mg, Al and Ti) in Lake Kinneret might be in a temperature range that is, with respect to the magnetization of the host rock, palaeomagnetically irrelevant, that is, below about 250 $^{\circ}$C. However, they might contribute to the magnetization of sediments. Chromium-magnetites represent only a small fraction of the studied Lake Kinneret sediments, therefore, thermomagnetic measurements are not suitable for detecting chromium-magnetites. Magnetic iron sulphides, as discussed later, also have Curie-temperatures below that of pure magnetite. Thus, only SEM/EDS techniques could demonstrate the presence of chromium-magnetites in the sediments of Lake Kinneret.

Magnetite spherules

In the four samples collected from the outer zone of the sediment core (Fig. 2), spherules of 40–60 μm diameter were found. Elemental analyses, various point and line scans, only have Fe and O peaks in their EDS data, which indicate that they consist of pure magnetite. Thus, the spherules are chemically and physically different from the octahedral or irregularly shaped lithogenic titanomagnetites that have a more variable composition (Mg, Al, Ti, Mn and Cr beside Fe). At low magnifications ($< \times 2000$) the spherules apparently have an orange peel-like structure (Plate 6a). At medium magnifications ($\times 5000$ to $\times 15\,000$) a dendritic structure can be resolved within the surface (Plate 6b). At high magnifications ($\times 50\,000$ to $\times 150\,000$), a layered dendrite structure becomes visible (Plate 6d). The individual layers have an estimated thickness of some 20–40 nm. The overall granular surface structure visible at the highest magnifications are due to a less optimally performed sputtering. Included in Plate 6 are results of an elemental line scan across a magnetite spherule. The bright flaky aggregates of submicron size (Plates 6b and c) are iron sulphides, which are interpreted to be greigite because of the relatively low S peak. These samples were sputtered with an Au/Pd alloy, therefore the main S peaks (Kα1 2.307 keV, Kα2 2.306 keV) are almost obscured by the Mα1 (2.123 keV), Mα2 (2.118 keV), and Mβ (2.205 keV) Au peaks associated with the sputtered coating. This makes it difficult to assess the stoichiometry of the iron sulphide. Some of the observed spherules are broken (Plate 6e) which reveals that they are hollow with a variable shell thickness.

Magnetite spherules with different origins have been described in literature. Frequently, magnetic spherules are found in environmental studies and are interpreted to be produced by steel plants, by fuel burning in cars, by coal burning in power plants, etc. (e.g. Puffer *et al.* 1980; Heller *et al.* 1998; Hoffmann *et al.* 1999; Jordanova *et al.* 2004; Veneva *et al.* 2004; Horng *et al.* 2009). Some spherules have a cosmogenic origin (e.g. Nriagu & Bowser 1969; Puffer *et al.* 1980; Taylor & Brownlee 1991; Stankowski *et al.* 2006), especially in cases where an anthropogenic origin can be clearly excluded, for example, when materials such as wüstite or cobalt and nickel in meteoritic proportions are incorporated (e.g. Marvin & Einaudi 1967). Cosmogenic spherules present within tektites have been found to contain a core of elemental iron and nickel (Kleinmann 1969). Diagenetic origins for certain magnetite spherules have also been discussed (e.g. McCabe *et al.* 1983).

To exclude an anthropogenic or industrial origin for the (hollow) magnetite spherules in the Kinneret sediments, the parallel set of five palaeomagnetic samples, collected from the centre of the core, was also analysed. Although from similar stratigraphic levels (Fig. 2), not a single magnetite spherule could be found in this material. Thus, the spherules within samples from the outer part of the core are assumed to be contaminants. The extracted material was in contact with the steel core barrel since coring. Therefore, it is likely that the spherules are of industrial origin, probably from the steel factory where the core barrels were produced. The spherules were probably removed from the core barrel wall during extrusion of the core.

Calcareous spherules (microfossils)

Spherical carbonate microfossils were found in all nine magnetic extracts. EDS data confirm that they all consist only of Ca, O and C (Plate 7). According to Almogi-Labin (Geol. Survey, Israel, personal communication, 2011) these calcareous microfossils are planktic foraminifera. No foraminifera currently live in the lake. However, during the period of time represented by the studied cores, three species of brackish benthic foraminifera were found in samples that were taken mainly from a trench at the Ohalo archaeological site. However, these species are not found in the magnetic extracts. Thus, the fossils in the studied samples are interpreted as being reworked from rocks that crop out in the Lake Kinneret catchment.

The foraminifera all have a relatively dark contrast in the backscatter images, especially when compared to titanomagnetites, which consist of heavier elements (*cf.* Plate 7f and corresponding EDS data set). The calcareous microfossils might normally be looked upon as contaminations in the magnetic extract. However, within the broken microfossil in Plate 7f, the bright patches are iron sulphides. This was confirmed by an additional polished section of a magnetic extract embedded in epoxy (Plate 8), which enabled probing of the interior of some microfossils in more detail. Inside the microfossils, massive pyrite and less dense aggregates of submicron greigite were found. The shells consist of calcium carbonate. Greigite smaller than 1 μm was also found inside a hollow siliceous sponge needle (Plate 8d). The observed calcareous microfossils, and some other organic remnants, such as in Plate 7f (upper right) and Plate 8d, therefore appear to have been attracted by the magnet because they have a magnetic core of greigite. Greigite has been commonly reported to have grown within foraminifera in marine sediments (e.g. Roberts & Turner 1993; Roberts *et al.* 2005; Rowan *et al.* 2009).

A large sulphide aggregate in the polished section in Plate 8e, also consists of granular greigite smaller than 1 μm together with massive pyrite. The two iron sulphides can be clearly distinguished from the height of the iron peak with respect to the sulphur peak in the EDS data, normalized to the sulphur peak. For verification, an ∼3 mm crystal of pyrite was crushed and was also analysed in the SEM/EDS using the same settings as for the magnetic extracts. The spectra obtained from the pyrite reference are similar to the red curves shown in Plate 8, with the iron peak height being about 20 per cent of the sulphur peak height. The yellow curves in Plate 8 indicate a significantly higher iron content, which indicate that the analysed grains are greigite. Results discussed so far provide further evidence for iron sulphide formation in Lake Kinneret sediments (see also pyrites in Plate 4). The iron sulphides are discussed below.

Iron sulphides

Probably the largest group of particles in the analysed extracts are iron sulphides (Plates 9–11). As already discussed in the context of analysed iron oxides, some of the iron sulphides (pyrite) occur as overgrowths on the surfaces of residual titanomagnetites, and on or within ilmenite skeletons (Plate 4). This indicates that the iron within the pyrite crystals was directly derived from the titanomagnetites upon which they grew, such as was also found by Canfield *et al.* (1992).

Other iron sulphides are associated with remnants of organic matter, as indicated by the presence of organic looking material around the iron sulphide aggregates, but also as clearly identified by elemental peaks mainly for carbon and oxygen (Plates 9 and 10). Associated iron sulphides are either present as ellipsoidal clusters (Plates 9a, b and e and Plates 10b and e) or as framboidal aggregates (Plates 9c and d, Plates 10c and d and Plates 11e.1 and e.2). Many of the sulphidic clusters, even at high magnifications, do not contain clear evidence of crystallization of their individual submicron, flaky particles (e.g. Plate 9b). The separate large egg-shaped, massive iron sulphide aggregate in Plate 9e probably also formed within an organic remnant, such as a plant cell vacuole, similar to what has been observed by van Dongen *et al.* (2007). In contrast to the massive sulphides in Plates 9b and e, framboidal iron sulphides are mostly made of 0.5–2 μm crystalline octahedra that are clearly visible in Plates 11e.1 and e.2. Irregularly arranged small iron sulphide octahedra (about 1–2 μm) were also found. These clusters are embedded in organic tissues (Plate 9f). The formation of iron sulphides is evidently linked to, or mediated by the presence of organic matter, although the observations do not give information on how exactly this process was controlled in the investigated samples. Iron sulphides in organic remnants have been reported also by, for example, Vallentyne (1963), who found pyrite inside pollen, higher plant cells and even within a fossil antennule of *Bosmina* (cladocera) in material extracted from sediments from Little Round Lake, Ontaria, Canada. Framboidal and non-framboidal pyrite and greigite have often been reported within the chambers of foraminifera (e.g. Roberts & Turner 1993; Roberts *et al.* 2005). Framboidal pyrite inside diatoms in sediments from Lake Challa, Kenya have also been reported by Kristen (2009). Roberts *et al.* (2010) also reported iron sulphides (greigite, pyrite) that crystalized inside remineralized plants cells.

Many further iron sulphides consist of cubic pyrite crystals and aggregates (Plate 11). The cubes, which are partly elongated along the [100] plane, often with additional [110] and [111] planes, are mainly in the size range of 10–20 μm, and have often grown together in relatively large aggregates of up to 150 μm in length (Plate 11b). The [100] planes of the pyrite cubes have a submicron cross-hatching, but sometimes an irregular pattern, which gives the cubes a porous appearance. In Plates 11e.1 and e.2, an euhedral pyrite cube seems to have partly overgrown a framboidal pyrite aggregate. Thus, the cubes are likely to represent the final stage of pyrite formation, which started with a framboidal phase (Plate 11e), or even with a (pseudo-) amorphous phase (Plates 9a and b). This interpretation is consistent with the interpretations of Raiswell (1982), supported by the SEM image in Plate 10b, where aggregates of both framboidal and cubically shaped pyrites are sited within the same piece of an organic (plant) remnant. The irregularly structured appearance of some cube [100] planes thus might be due to incorporated multiple pyrite octahedra (Plate 11d) that originally formed a framboidal aggregate. Nevertheless, it is worth considering why aggregates as large as 150 μm of non-magnetic pyrite were attracted by the magnetic extraction probes. One possible explanation is evidenced directly from Plate 4: many residual titanomagnetites and skeletal ilmenites are largely overgrown by pyrite (*cf.* Canfield & Berner 1987). Thus, the magnetic moment of a titanomagnetite remnant inside a larger pyrite aggregate might be strong enough to be attracted by the strong magnetic extraction probes. Furthermore, XRD analyses on extracts KIN5A-1 to 4 indicate the presence of 14 to 24 per cent greigite, 7 to 26 per cent pyrite, and just 2 to 4 per cent (titano-) magnetite (Ron *et al.* 2007). Therefore, it can be concluded that the iron sulphides, interpreted from their cubical shape to be non-magnetic pyrite, might contain cores consisting of ferrimagnetic greigite, which makes them magnetically attractable. This inference is consistent with observations of Rowan & Roberts (2006) who found a greigite framboid rimmed by pyrite in Neogene marine sediments from New Zealand. In contrast, a pyrite powder

of 1–20 μm particles (checked with SEM imaging), prepared by crushing a pure 3 mm pyrite crystal with mortar and pestle, was not attracted at all by the extraction probes used for Lake Kinneret sediments. This provides indirect evidence that magnetically extracted particles, such as shown in Plate 11, with a superficial composition of pyrite, are likely not completely composed of pyrite inside. For example, the EDS data for the cube in Plate 11c contain an iron peak that is higher than would be expected from pure pyrite (see Plate 8).

In summary, images of iron sulphide aggregates provide clear evidence that they formed diagenetically as secondary minerals at the expense of primary detrital titanomagnetites. Their formation was evidently mediated by the presence of organic matter. According to Raiswell (1982) the type of formation of pyrite is controlled by the availability of iron and the degree of supersaturation of iron monosulphides and pyrite during the evolution of pore waters. Thus, euhedral crystals form directly at lower degrees of supersaturation such that pyrite is supersaturated and iron monosulphides are undersaturated. This framework supports the observations in which framboidal sulphides are overgrown by euhedral pyrite.

DISCUSSION

As summarized by Berner (1984), pyritization in sediments results from the interaction of organic matter, sulphide reducing bacteria, available sulphate, dissolved iron and concomitantly produced H_2S. The simplified sequence can be summarized as follows: amorphous iron sulphide → mackinawite → greigite → pyrite (see, e.g. Raiswell 1982). For tidal sediments, Ivarson & Hallberg (1976) described the microbial reduction of jarosite ($KFe_3(SO_4)_2(OH)$) that has previously been formed by the aerobic iron-oxidizing bacterium *Thiobacillus ferrooxidans*, into mackinawite, under anaerobic conditions and in the presence of organic matter, by the sulphate-reducing bacterium *Desulfovibrio desulfuricans*. Mackinawite is a tetragonal iron sulphide (Berner 1962). According to Rickard *et al.* (2007) mackinawite has the composition $Fe_{1.00\ \pm 0.01}S$. Greigite (Fe_3S_4), the thio-spinel of iron (Skinner *et al.* 1964), has ferrimagnetic properties comparable to magnetite. Due to their similar crystallographic structures, cubic greigite can easily be formed out of tetragonal mackinawite (FeS) by oxidation of two-thirds of the Fe(II) of mackinawite to Fe(III) in the greigite (e.g. Taylor *et al.* 1979; Lennie *et al.* 1997; Rickard & Luther III 2007). According to Benning *et al.* (2000) slightly oxidizing environments are necessary for the conversion of mackinawite into pyrite, with greigite as an intermediate product. Sweeney & Kaplan (1973) also stated that during laboratory synthesis greigite converted into pyrite only when oxygen was available in the vessels. Mackinawite has always been reported as a pre-existing phase in greigite syntheses (Rickard & Luther III 2007). Hunger & Benning (2007) showed that growth of greigite and pyrite under hydrothermal conditions is accomplished by oriented aggregation of nanoparticulate mackinawite and pyrite, respectively.

Since it has been observed that in many pyrite framboids the individual crystals seem to have a similar grain size, Wilkin & Barnes (1997) concluded that there is a four-step development of pyrite framboids: (1) a (single) initial nucleation event and growth of iron monosulphide (mackinawite), (2) reaction of the initial monosulphide to greigite, (3) aggregation of greigite microcrystals and (4) replacement of greigite by pyrite. Butler & Rickard (2000) concluded that formation of framboidal pyrite might be explained by a rapid nucleation in environments where pyrite is supersaturated and that framboid formation can proceed without an intermediate (magnetic) phase of greigite. Kao *et al.* (2004) provided evidence that the intermediate greigite can be preferentially preserved when the supply of reactive (reducible) iron exceeds availability of dissolved sulphide.

Because magnetic particles represent only about one per mill, or even less, of the bulk sediment, detailed inspection by electron microscope imaging appears to be much easier when the particles are magnetically concentrated. However, because the sediment is resuspended, the magnetic extraction process removes the remanence carriers out of their sedimentary context. This is especially a disadvantage for analysing dissolution of primary iron oxides and formation of secondary iron sulphides associated with the degradation of organic matter, as is the case in the studied sediments from Lake Kinneret. Polished sections of complete sediment samples, such as investigated by Weaver *et al.* (2002) and Roberts & Weaver (2005) can be an alternative, if the concentration of magnetic minerals is not too low. Nevertheless, the images presented in this paper provide visual confirmation of many of the magnetic mineral transformations that occur in reducing diagenetic environments.

CONCLUSIONS

Submerging plastic-covered magnets into sediment-alcohol slurries enabled extraction of magnetic particles for analysis of the impact of diagenetic magnetite dissolution on sediments from Lake Kinneret. Although mainly larger particles (>2 μm) were extracted, SEM imaging and EDS analyses yielded detailed and explicit information about the magnetic mineral inventory, its composition and state of preservation. Nearly all titanomagnetites and titanomaghemites, among which the latter are characterized by shrinkage cracks, contain evidence of severe etching and dissolution. Some crystals have had their lattice destroyed by etching, leaving sponge-like features or grain fragments (Plates 2 and 3), but many others are residual structures consisting of ilmenite lamellae that originally evolved within the primary igneous rocks by low-temperature exsolution from the titanomagnetite (Plate 4). Often, the space between the brittle 0.1–1.0 μm thin platelets is empty. Ilmenite largely resisted the etching in the inferred anoxic diagenetic environment. The released iron from the dissolved magnetite was used to form iron sulphides that were frequently detected in the extracts. Pyrite crystals often directly reside on massively etched residual ilmenite skeletons (Plate 4c). Other particles are encrusted by pyrite. Both ilmenite and pyrite are non-magnetic. Thus a small remaining core of titanomagnetite inside many particles, which is sufficiently protected by nested ilmenite lamellae, must be assumed to explain why the grains were attracted during extraction.

In addition to enriching magnetic particles via magnetic extraction, other (apparently) non-magnetic minerals were also magnetically extracted. These sometimes were large (>150 μm) pyrite crystals, or more generally, iron sulphide particles and/or aggregates. Three different types of sulphide particles were observed: first, 10–20 μm ellipsoidal aggregates consisting of flaky, submicron particles without clearly detectable crystallographic surfaces; second, 1–2 μm octahedra, either irregularly distributed within organic remnants, or, arranged in framboids up to 10 μm in diameter; and third, cubic 20 μm pyrite crystals, sometimes forming aggregates up to 150 μm in length. In many cases, these iron sulphides are associated with organic matter, which acted as a mediator for sulphidization reactions. The presence of highly concentrated greigite, mostly in the magnetically single domain size range, was confirmed

by thermomagnetic and hysteresis measurements, respectively (Ron *et al.* 2007). Thus, it is concluded that the large iron sulphide aggregates contain greigite, probably as cores within the pyrite structures. Several organic remnants contain small bright spots in backscatter images, which are iron sulphides (e.g. Plate 7f), possibly greigite.

Chromium-magnetites, which probably originated from alkaline-basalts exposed around Lake Kinneret, are frequently found in all extracts, and have a significantly better state of preservation compared to titanomagnetites. Their Cr contents indicate that they might play a role as a remanence carrier. However, they do not dominate the magnetic fraction, and their (thermo-) magnetic properties overlap with those of titanomagnetite and greigite, respectively. Thus, it was not possible to detect their presence using rock magnetic analyses (Ron *et al.* 2007).

Magnetite spherules found only in extracts from the outer zone of the sediments represent contamination resulting from direct contact with the steel core liner. Material from the central part of the sediment core is completely devoid of such spherules.

In summary, detailed analyses of magnetic extracts using SEM imaging and EDS analyses can provide valuable information about the identity of magnetic minerals, their state of preservation and partly also their genesis. However, only observations from polished sections preserving the original sedimentary context allow additional interpretations concerning fluid-solid interactions. In the case of the studied Lake Kinneret sediments, the obtained information illustrates how diagenetic dissolution has destroyed primary remanence carriers and how secondary iron sulphides have evolved from the released iron.

ACKNOWLEDGMENTS

I thank M. Voigt who provided the excellent iron fingers and plastic hoses for the magnetic extraction probes and G. Anold who prepared the polished section. H. Kemnitz, J. Herwig and I. Schäpan are acknowledged for their technical support at the SEM/EDS facility. N.J. Zaluzec from Microscopy.com kindly provided a data base with X-ray transition energies for reference. Finally I thank the reviewers, and especially A. Roberts for his detailed comments, which significantly improved the quality of this paper.

REFERENCES

Barnes, S.J. & Roeder, P.L., 2001. The range of spinel compositions in terrestrial mafic and ultramafic rocks, *J. Petrol.,* **42,** 2279–2302.

Bartov, Y., Stein, M., Enzel, Y., Agnon, A. & Reches, Z., 2002. Lake-levels and sequence stratigraphy of Lake Lisan, the Late Pleistocene precursor of the Dead Sea, *Quat. Res.,* **57,** 9–21.

Benning, L.G., Wilkin, R.T. & Barnes, H.L., 2000. Reaction pathways in the Fe-S system below 100 °C, *Chem. Geol.,* **167,** 25–51.

Berner, R.A., 1962. Tetragonal iron sulfide, *Science,* **137,** 669.

Berner, R.A., 1984. Sedimentary pyrite formation: an update, *Geochim. Cosmochim. Acta,* **48,** 605–615.

Butler, I.B. & Rickard, D., 2000. Framboidal pyrite formation via the oxidation of iron (II) monosulfide by hydrogen sulfide, *Geochim. Cosmochim. Acta,* **64,** 2665–2672.

Canfield, D.E. & Berner, R.A., 1987. Dissolution and pyritization of magnetite in anoxic marine sediments, *Geochim. Cosmochim. Acta,* **51,** 645–659.

Canfield, D.E., Raiswell, R. & Bottrell, S., 1992. The reactivity of sedimentary iron minerals toward sulfide, *Am. J. Sci.,* **292,** 659–683.

Channell, J.E.T. & Hawthorne, T., 1990. Progressive dissolution of titanomagnetites at ODP Site 653 (Tyrrhenian Sea), *Earth planet. Sci. Lett.,* **96,** 469–480.

Cui, Y., Verosub, K.L. & Roberts, A.P., 1994. The effect of low-temperature oxidation on large multi-domain magnetite, *Geophys. Res. Lett.,* **21,** 757–760.

Dekkers, M.J., Langereis, C.G., Vriend, S.P., van Santfoort, P.J.M. & de Lange, G.J., 1994. Fuzzy c-mean cluster analysis of early diagenetic effects on natural remanent magnetisation acquisition in a 1.1 Myr piston core from the Central Mediterranean, *Phys. Earth planet. Inter.,* **85,** 155–171.

van Dongen, B., Roberts, A.P., Schouten, S., Jiang, W.-T., Florindo, F. & Pancost, R.D., 2007. Formation of iron sulphide nodules during anaerobic oxidation of methane, *Geochim. Cosmochim Acta,* **71,** 5155–5167.

Francombe, M.H., 1957. Lattice changes in spinel-type iron chromites, *J. Phys. Chem. Solids,* **3,** 37–43.

Gehring, A.U., Fischer, H., Louvel, M. Kunze, K. & Weidler, P.G., 2009. High-temperature stability of natural maghemite: a magnetic and spectroscopic study, *Geophys. J. Int.,* **179,** 1361–1371.

Hazan, N., Stein, M., Agnon, A., Marco, S., Nadael, D., Negendank, J.F.W., Schwab, M.J., & Neev, D., 2005. The late quaternary limnology history of Lake Kinneret (Sea of Galilee, Israel), *Quat. Res.,* **63,** 60–77.

Heller, F., Strzyszsc, Z. & Magiera, T., 1998. Magnetic record of industrial pollution in forest soils in Upper Silesia, Poland, *J. geophys. Res.,* **103,** 17 767–17 774.

Hoffmann, V., Knab, M. & Appel, E., 1999. Magnetic susceptibility mapping of road side pollution, *J. geochem. Expl.,* **66,** 313–326.

Horng, C.-S., Huh, C.-A., Chen, K.-H., Huang, P.-R. Hsiung, K.-H. & Lin, H.-L., 2009. Air pollution history elucidated from anthropogenic spherules and their magnetic signatures in marine sediments offshore of Southwestern Taiwan, *J. Mar. Syst.,* **76,** 468–478.

Hounslow, M.W., 1996. Ferrimagnetic Cr and Mn spinels in sediments: residual magnetic minerals after diagenetic dissolution, *Geophys. Res. Lett.,* **23,** 2823–2826.

Hounslow, M.W. & Maher, B.A., 1999. Laboratory procedures for quantitative extraction and analysis of magnetic minerals from sediments, in *Environmental Magnetism: A Practical Guide*, pp. 139–184, eds Walden, J., Oldfield, F. & Smith, J.P., Quaternary Research Association, Cambridge.

Hunger, S. & Benning, L.G., 2007. Greigite: a true intermediate on the polysulfide pathway to pyrite, *Geochem. Trans.,* **8,** 1, doi:10.1186/1467-4866-8-1.

Ivarson, K.C. & Hallberg, R.O., 1976. Formation of mackinawite by the microbial reduction of jarosite and its application to tidal sediments, *Geoderma,* **16,** 1–7.

Johnson, H.P. & Merrill, R.T., 1973. Low-temperature oxidation of a titanomagnetite and the implications for paleomagnetism, *J. geophys. Res.,* **78,** 4938–4949.

Jordanova, D., Hoffmann, V. & Fehr, K.T., 2004. Mineral magnetic characterization of anthropogenic magnetic phases in the Danube river sediments (Bulgarian part), *Earth planet. Sci. Lett.,* **221,** 71–89.

Kao, S.-J., Horng, C-S., Roberts, A.P. & Liu, K.K., 2004. Carbon-sulfur-iron relationships in sedimentary rocks from southwestern Taiwan: influence of geochemical environment on greigite and pyrrhotite formation, *Chem. Geol.,* **203,** 153–168.

Karlin, R., 1990a. Magnetite diagenesis in marine sediments from the Oregon continental margin, *J. geophys. Res.,* **95,** 4405–4419.

Karlin, R., 1990b. Magnetic mineral diagenesis in suboxic sediments at Bettis Site W-N, NE Pacific Ocean, *J. geophys. Res.,* **95,** 4421–4436.

Karlin, R. & Levi, S., 1983. Diagensis of magnetic minerals in recent haemipelagic sediments, *Nature,* **303,** 327–330.

Karlin, R., Lyle, M. & Heath, R., 1987. Authigenic magnetite formation in suboxic marine sediments, *Nature,* **326,** 490–493.

Kleinmann, B., 1969. Magnetite bearing spherules in tektites, *Geochim. Cosmochim. Acta,* **33,** 1113–1120.

Kontny, A., Woodland, A.B. & Koch, M., 2004. Temperature-dependent magnetic susceptibility behaviour of spinelloid and spinel solid solutions

in the system Fe_2SiO_4-Fe_3O_4 and $(Fe,Mg)_2SiO_4$-Fe_3O_4, *Phys. Chem. Min.,* **31,** 28–40.

Kristen, I., 2009. Investigations on rainfall variability during the late Quaternary based on geochemical analyses of lake sediments from tropical and subtropical southern Africa, *PhD thesis*, University of Potsdam, doi:10.2312/GFZ.b103-10018.

Larrasoaña, J.C., Roberts, A.P., Stoner, J.S., Richter, C. & Wehausen R., 2003. A new proxy for bottom-water ventilation in the eastern Mediterranean based on diagenetically controlled magnetic properties of sapropel-bearing sediments, *Palaeogeog. Palaeoclimat. Palaeoecol.,* **190,** 221–242.

Lattard, D., Engelmann, R., Kontny, A. & Sauerzapf, U., 2006. Curie temperature of synthetic titanomagnetites in the Fe-Ti-O system: effects of composition, crystal chemistry, and thermomagnetic methods, *J. geophys. Res.,* **111,** B12S28, doi: 10.1029/2006JB004591.

Lennie, A.R., Redfern, S.A.T., Champness, P.E., Stoddart, C.P., Schofield, P.F. & Vaughan, D.J., 1997. Transformation of mackinawite to greigite: an in situ X-ray powder diffraction and transmission electron microscope study, *Am. Mineral.,* **82,** 302–309.

Leslie, B.W., Hammond, D.E., Berelson, W.M. & Lund, S.P., 1990a. Diagenesis in anoxic sediments from the California continental borderland and its influence on iron, sulfur, and magnetic behaviour, *J. geophys. Res.,* **95,** 4453–4470.

Leslie, B.W., Lund, S.P. & Hammond, D.E., 1990b. Rock magnetic evidence for the dissolution and authigenic growth of magnetic minerals within anoxic marine sediments of the California continental borderland, *J. geophys. Res.,* **95,** 4437–4452.

Marvin, U.B. & Einaudi, M.T., 1967. Black, magnetic spherules from Pleistocene and recent beach sands, *Geochim. Cosmochim. Acta,* **81,** 1871–1884.

McCabe, C., van der Voo, R., Peacor, D.R., Scotese, C.R. & Freeman, R., 1983. Diagenetic magnetite carries ancient yet secondary remanence in some Paleozoic sedimentary carbonates, *Geology,* **11,** 221–223.

Minyuk, P.S., Brigham-Grette, J., Melles, M., Borkhodoev, V.Y. & Glushkova, O.Y., 2007. Inorganic geochemistry of El'gygytgyn lake sediments (Northeastern Russia) as an indicator of paleoclimate change for the last 250 kyr, *J. Paleolimnol.,* **37,** 123–133.

Nriagu, J.O. & Bowser, C.J., 1969. The magnetic spherules in sediments of Lake Mendota, Wisconsin, *Water Res.,* **3,** 833–842.

Nowaczyk, N.R., Harwart, S. & Melles, M., 2000. A rock magnetic record from Lama Lake, Taymyr Peninsula, Northern central Siberia, *J. Paleolimnol.,* **23,** 227–241.

Nowaczyk, N.R. *et al*., 2002. Magnetostratigraphic results from impact crater Lake El'gygytgyn, northeastern Siberia: a 300 kyr long high-resolution terrestrial palaeoclimatic record from the Arctic, *Geophys. J. Int.,* **150,** 109–126.

Nowaczyk, N.R., Melles, M. & Minyuk, P.S., 2007. A revised age model for core PG1351 from Lake El'gygytgyn, Chukotka, based on magnetic susceptibility variations tuned to northern hemisphere insolation variations, *J. Paleolimnol.,* **37,** 65–76.

Petersen, N. & Vali, H., 1987. Observation of shrinkage cracks in ocean floor titanomagnetites, *Phys. Earth planet. Inter.,* **46,** 197–205.

Puffer, J.H., Russell, E.W.B. & Rampino, M.R., 1980. Distribution and origin of magnetite spherules in air, waters, and sediments of the greater New York City area and the North Atlantic Ocean, *J. Sediment. Petrol.,* **50,** 247–256.

Raiswell, R., 1982. Pyrite texture, isotopic composition and the availability of iron, *Am. J. Sci.,* **282,** 1244–1263.

Richards, J.C.W., O'Donovan, J.B., Hauptman, Z., O'Reilly, W. & Creer, K.M., 1973. A magnetic study of titanomagnetite substituted by magnesium and aluminium, *Phys. Earth planet. Inter.,* **7,** 437–444.

Rickard, D. & Luther G.W. III, 2007. Chemistry of iron sulfides, *Chem. Rev.,* **107,** 514–562.

Rickard, D., Griffith, A., Oldroyd, A., Butler, I.B., Lopez-Capel, E., Manning, D.A.C. & Apperley, D.C., 2007. The composition of nanoparticulate mackinawite, tetragonal iron(II) monosulfide, *Chem. Geol.,* **235,** 286–298.

Robbins, M., Wertheim, G.K., Sherwood, R.C. & Buchanan, D.N.E., 1971. Magnetic properties and site distributions in the system $FeCr_2O_4$-Fe_3O_4 ($Fe^{2+}Cr_{2-x}Fe_x^{3+}O^4$), *J. Phys. Chem. Solids,* **32,** 717–729.

Roberts, A.P. & Turner, G.M., 1993. Diagenetic formation of ferrimagnetic iron sulphide minerals in rapidly deposited marine sediments, South Island, New Zealand, *Earth planet. Sci. Lett.,* **115,** 257–273.

Roberts, A.P. & Weaver, R., 2005. Multiple mechanisms of remagnetization involving sedimentary greigite (Fe3S4), *Earth planet. Sci. Lett.,* **231,** 263–277.

Roberts, A.P., Jiang, W.-T., Florindo, F., Horng, C.-S. & Laj, C., 2005. Assessing the timing of greigite formation and the reliability of the Upper Olduvai polarity transition record from the Crostolo River, Italy, *Geophys. Res. Lett.,* **32,** L05307, doi:10.1029/2004GL022137.

Roberts, A.P., Florindo, F., Larrasoaña, J.C., O'Regan, M.A. & Zhao, X., 2010. Complex polarity pattern at the former Plio–Pleistocene global stratotype section at Vrica (Italy): remagnetization by magnetic iron sulphides, *Earth planet. Sci. Lett.,* **292,** 98–111.

Roberts, A.P., Chang, L., Rowan, C.J., Horng, C.-S. & Florindo, F., 2011. Magnetic properties of sedimentary greigite (Fe3S4): an update, *Rev. Geophys.,* **49,** RG1002, doi:10.1029/2010RG000336.

Ron, H., Nowaczyk, N.R., Frank, U., Schwab, M.J., Naumann, R., Striewski, B. & Agnon, A., 2007. Greigite detected as dominating remanence carrier in Late Pleistocene sediments, Lisan Formation, from Lake Kinneret (Sea of Galilee), Israel, *Geophys. J. Int.,* **170,** 117–131.

Rowan, C.J., & Roberts, A.P., 2006. Magnetite dissolution, diachronous greigite formation, and secondary magnetizations from pyrite oxidation: unravelling complex magnetizations in Neogene marine sediments from New Zealand, *Earth planet. Sci. Lett.,* **241,** 119–137.

Rowan, C.J., Roberts, A.P. & Broadbent, T., 2009. Reductive diagenesis, magnetite dissolution, greigite growth and paleomagnetic smoothing in marine sediments: a new view, *Earth planet. Sci. Lett.,* **277,** 223–235.

Schmidtbauer, E., 1983. Magnetization of Fe-Cr-Ti spinels, *Phys. Chem. Min.,* **9,** 124–126.

Skinner, B.J., Erd, R.C. & Grimaldi, F.S., 1964. Greigite, the thiospinel of iron: a new mineral, *Am. Mineral.,* **49,** 543–555.

Stankowski, W.T.J., Katrusiak, A. & Budzianowski, A., 2006. Crystallographic variety of magnetic spherules from Pleistocene and Holocene sediments in the northern foreland of Morasko-Meteorite Reserve, *Planet. Space Sci.,* **54,** 60–70.

Sweeney, R.E. & Kaplan, I.R., 1973. Pyrite framboid formation: laboratory synthesis and marine sediments, *Econ. Geol.,* **68,** 618–634.

Taylor, S. & Brownlee, D.E., 1991. Cosmic spherules in the geological record, *Meteoritics,* **26,** 203–211.

Taylor, P., Rummery, T.E. & Owen, D.G., 1979. On the conversion of mackinawite to greigite, *J. Inorg. Nucl. Chem.,* **41,** 595–596.

Vahle, C., Kontny, A., Gunlaugsson, P.P. & Kristjansson, L., 2007. The Stardalur magnetic anomaly revisited-new insights into a complex cooling and alteration history, *Phys. Earth planet. Inter.,* **164,** 119–141.

Vallentyne, J.R., 1963. Isolation of pyrite spherules from recent sediments, *Limnol. Oceanogr.,* **8,** 16–30.

Veneva, L., Hoffmann, V., Jordanova, D., Jordanova, N. & Fehr, T., 2004. Rock magnetic, mineralogical and microstructural characterization of fly ashes from Bulgarian power plants and the nearby anthropogenic soils, *Phys. Chem. Earth,* **29,** 1011–1023.

Wasilewski, P.J., Thomas, H.H. & Mayhew, M.A., 1979. The Moho as a magnetic boundary, *Geophys. Res. Lett.,* **6,** 541–544.

Weaver, R., Roberts, A.P. & Barker, A.J., 2002. A late diagenetic (syn-folding) magnetization carried by pyrrhotite: implications for paleomagnetic studies from magnetic iron sulphide-bearing sediments, *Earth planet. Sci. Lett.,* **200,** 371–386.

Wilkin, R.T. & Barnes, H.L., 1997. Formation processes of framboidal pyrite, *Geochim. Cosmochim. Acta,* **61,** 323–339.

Zhou, W., Van der Voo, R., Peacor, D.R., Wang, D. & Zhang, Y., 2001. Low-temperature oxidation in MORB of titanomagnetite to titanomaghemite: a gradual process with implications for marine magnetic anomaly amplitudes, *J. geophys. Res.,* **106,** 6409–6421.

Plate 1. Various well-preserved (titano-) magnetites: (a) and (b) nearly idomorphic (octahedral) grains, (c) and (d) irregularly shaped grains, (e) and (f) particles with shrinkage-cracks that provide evidence for maghemitization. Spots for X-ray element analyses (bottom) are indicated by coloured circles. The same is the case for all succeeding plates. BSc, backscattered electrons; InL, Inlens detector.

Plate 2. Etching features in two titanomagnetite grains that provide evidence for diagenetic dissolution. The close-ups in (b) and (c) reveal that the grain in (a) is very porous, and the close-ups in (e) and (f) reveal deep cracks and cavities of the brittle grain in (d) that already started to disintegrate. InL, Inlens detector.

Plate 3. Traces of pervasive etching in three titanomagnetites/maghemites. Like the grains in Plate 2, the brittle grains have partly disintegrated and have (c) sponge-like features and (f) pitting corrosion. SE, secondary electrons; InL, Inlens detector.

Plate 4. (a) An idiomorphic and well-preserved titanomagnetite compared to (b)–(f) four residual, skeletal titanomagnetites, which consist only of ilmenite lamellae, oriented parallel to the octahedral [111] planes. Particles in (c)–(f) are partly overgrown by pyrite, as indicated by the yellow EDS curve corresponding to analyses of (c). BSc, backscattered electrons.

Plate 5. Examples of six mostly well-preserved, idiomorphic (octahedral) chromium-magnetites. All analysed chromium-magnetites have significant Mg, Al and Ti contents (bottom), which indicate complex solid solutions of magnetite (Fe_3O_4), ulvöspinel ($TiFe_2O_4$), chromite ($FeCr_2O_4$) and spinel ($MgAl_2O4$) in the original igneous source rocks. SE, secondary electrons; BSc, backscattered electrons; InL, Inlens detector.

Plate 6. Magnetite spherules extracted from the outer part of the sediment core that was in contact with the steel core barrel. Some spherules are broken, which reveals that they are hollow (e). Sediment from the centre of the core (see Fig. 2) is completely free of such spherules, which are therefore interpreted to be a technical contaminant, and not of cosmogenic or other origin. Elemental analyses indicate that the spherules only consist of iron and oxygen, which is interpreted to be magnetite. Bright patches in (a)–(d) are iron sulphides, most likely greigite that was attracted to the magnetic sphere. 'Au' together with vertical yellow bars indicate X-ray emission lines from the Au/Pd sputter material. SE, secondary electrons; InL, Inlens detector.

Plate 7. Calcareous microfossils found in the magnetic extracts. The spherules which consist of relatively light elements (C, O and Ca) are relatively dark in the backscatter images compared to titanomagnetite and iron sulphides which are dominated by heavier elements (Ti, Mn and Fe), as evidenced by EDS data in (f). SE, secondary electrons; BSc, backscattered electrons; InL, Inlens detector.

Plate 8. SEM images and corresponding EDS data (normalized to respective maximum) from a thin section prepared from a magnetic extract. Some of the chambers of calcareous microfossils (a)–(c) are filled either with granular greigite (yellow circle/curve) or massive pyrite (red circle/curve). A hollow siliceous sponge needle (d) has a granular greigite filling. The iron sulphide cluster in (e) consists of submicron sized greigite crystals (yellow circle/curve) and massive pyrite (red circle/curve). BSc, backscattered electrons.

Plate 9. Ellipsoidal aggregates of nano-crystalline iron sulphides (a) and (b) attached to, or (c) and (d) embedded in organic remnants, (e) isolated ellipsoidal iron sulphide aggregate, and (f) irregularly arranged but crystalline pyrite octahedra, about 2 μm in size, embedded in an organic matrix. BSc, backscattered electrons; InL, Inlens detector.

Plate 10. Overview of (a) a large, 700 μm plant remnant, containing different types of iron sulphide aggregates within its elongated pore spaces, (b) close-up of the fibrous structure with 20 μm, well-developed pyrite crystals and aggregates, visible in the lower part of the image, (c) and (d) close-ups of about 0.3 μm particles forming 2–3 μm framboidal substructures, (e) and (f) close-ups of an unstructured, about 40 μm ellipsoidal iron sulphide cluster of about 0.3 μm particles/crystals. BSc, backscattered electrons, InL, Inlens detector.

Plate 11. Typical aggregates of 10 to 20 μm pyrite crystals. Beside the cubic [100] plane, often also the [110] and [111] planes are developed, and the crystals can be elongated along [100], such as in (c) and (d). However, the surface structure of the pyrite crystals indicates a porous habit and/or inhomogeneous composition. The dashed lines in the backscatter (BSc) view of the framboid cluster in (e.1) mark particles that moved away while the SEM was prepared for another (InL, inlens) view of the same structure (e.2). This particular aggregate also contains larger, incomplete cubic pyrite crystals that have overgrown framboids, thus probably illustrating the transition from framboidal to cubic growth of pyrite in the investigated sediments. BSc, backscattered electrons; InL, Inlens detector.

Plate 1

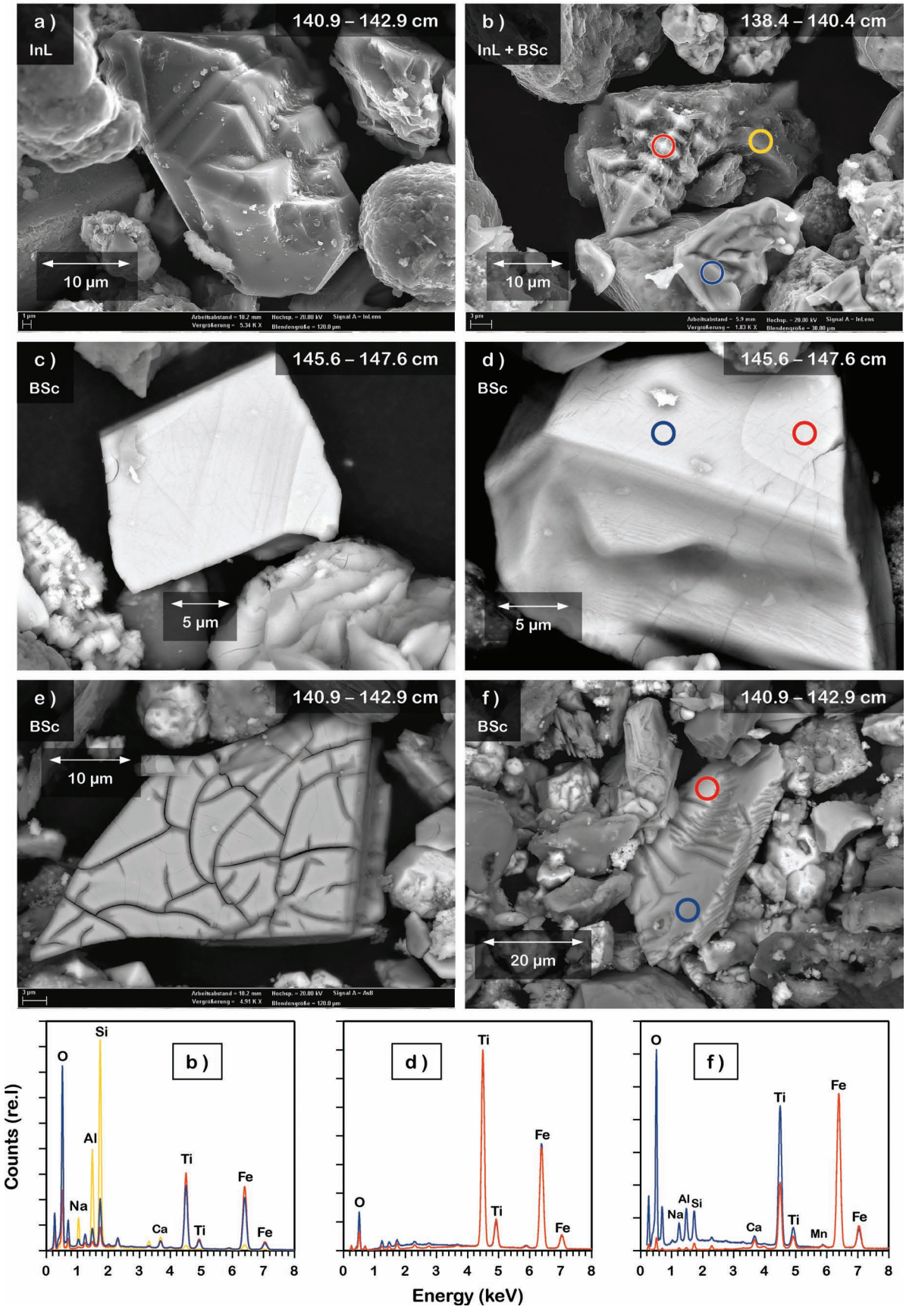
a)
InL
140.9 – 142.9 cm
10 µm
b)
InL + BSc
138.4 – 140.4 cm
10 µm
c)
BSc
145.6 – 147.6 cm
5 µm
d)
BSc
145.6 – 147.6 cm
5 µm
e)
BSc
140.9 – 142.9 cm
10 µm
f)
BSc
140.9 – 142.9 cm
20 µm
b)
O
Si
Al
Na
Ca
Ti
Ti
Fe
Fe
d)
O
Ti
Ti
Fe
Fe
f)
O
Ti
Fe
Al
Si
Na
Ca
Ti
Mn
Fe
Counts (re.l)
0 1 2 3 4 5 6 7 8
Energy (keV)

Plate 2

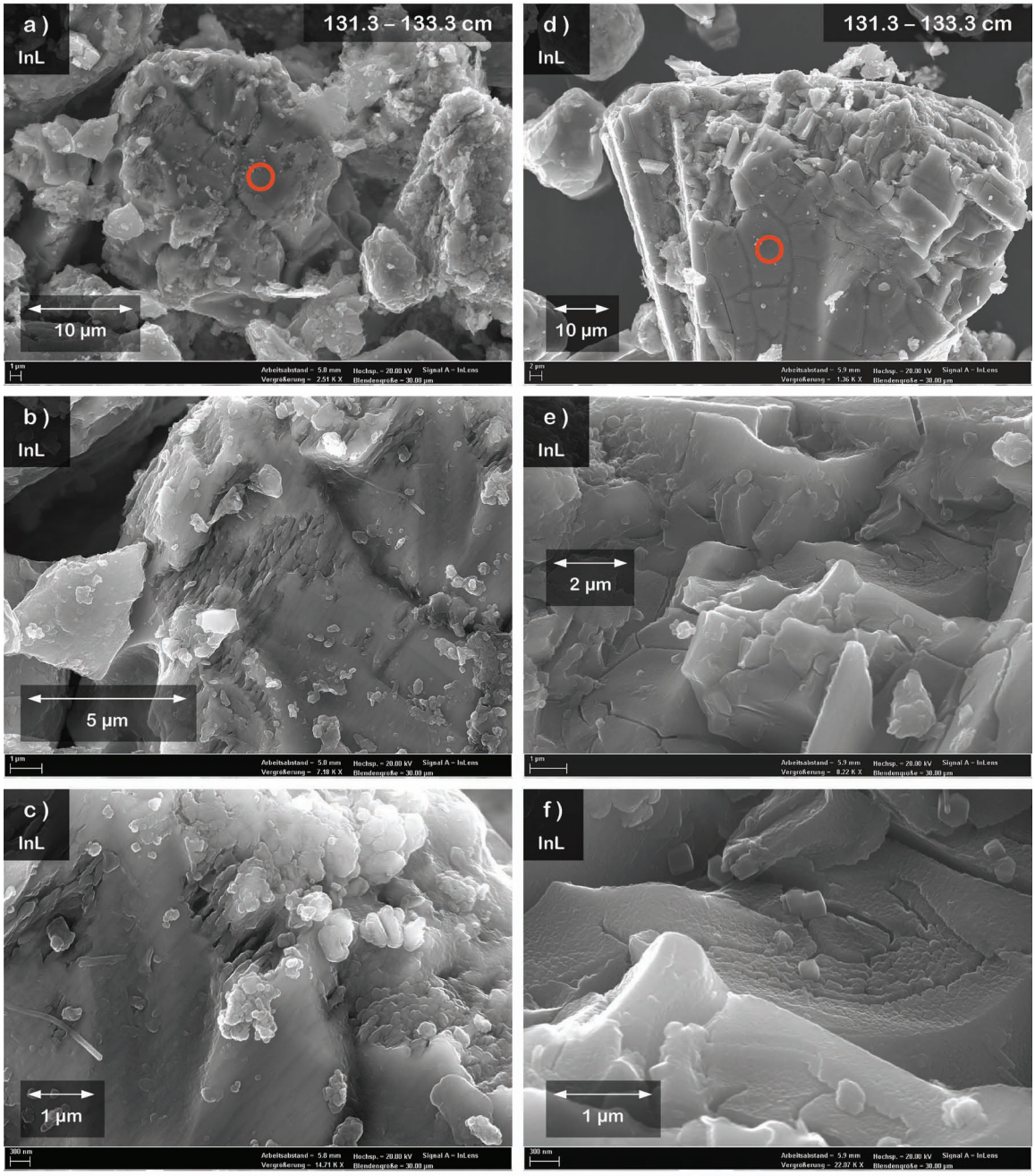
a)
InL
131.3 – 133.3 cm
10 µm
d)
InL
131.3 – 133.3 cm
10 µm
b)
InL
5 µm
e)
InL
2 µm
c)
InL
1 µm
f)
InL
1 µm

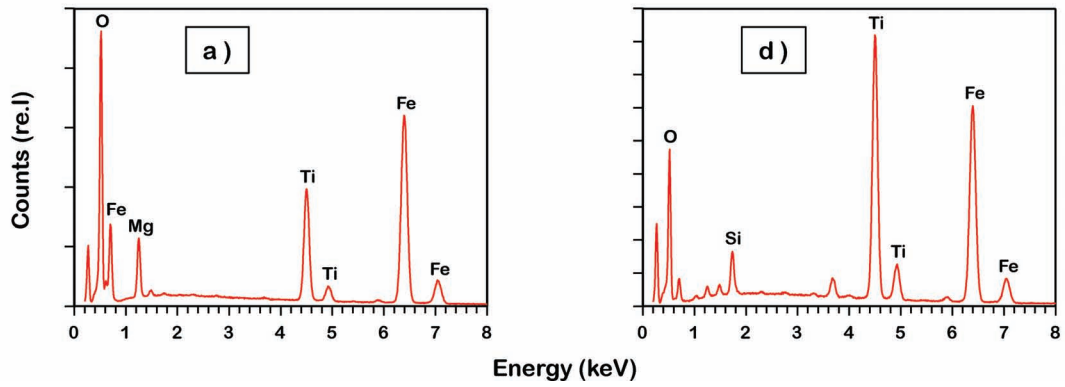
a)
O
Fe
Mg
Ti
Ti
Fe
Fe
d)
Ti
O
Si
Ti
Fe
Fe
Counts (re.l)
0 1 2 3 4 5 6 7 8
Energy (keV)

Plate 3

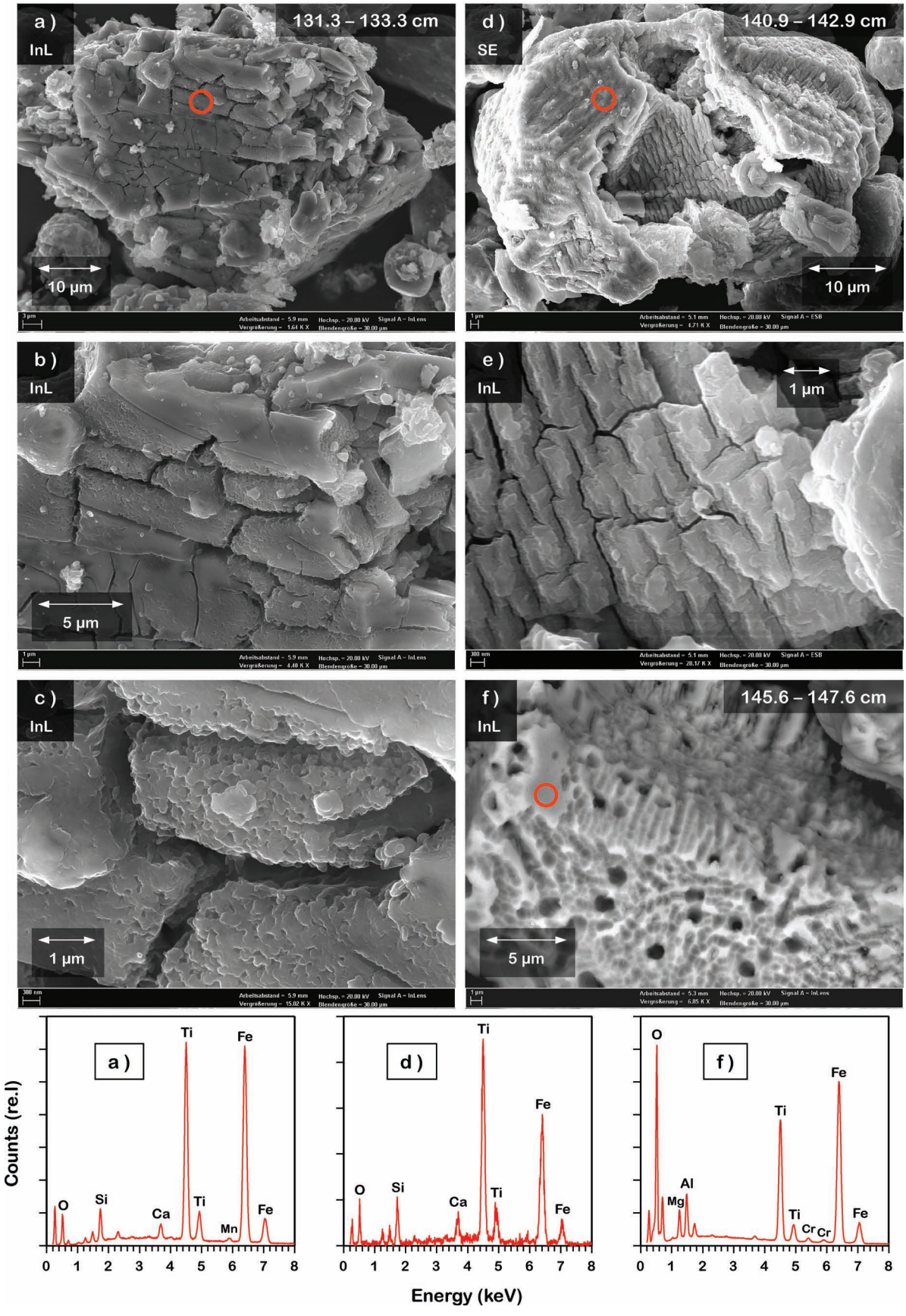
a)
InL
131.3 – 133.3 cm
10 µm
d)
SE
140.9 – 142.9 cm
10 µm
b)
InL
5 µm
e)
InL
1 µm
c)
InL
1 µm
f)
InL
145.6 – 147.6 cm
5 µm
a)
d)
f)
Counts (re.l)
Energy (keV)
O
Si
Ca
Ti
Mn
Fe
Mg
Al
Cr

Plate 4

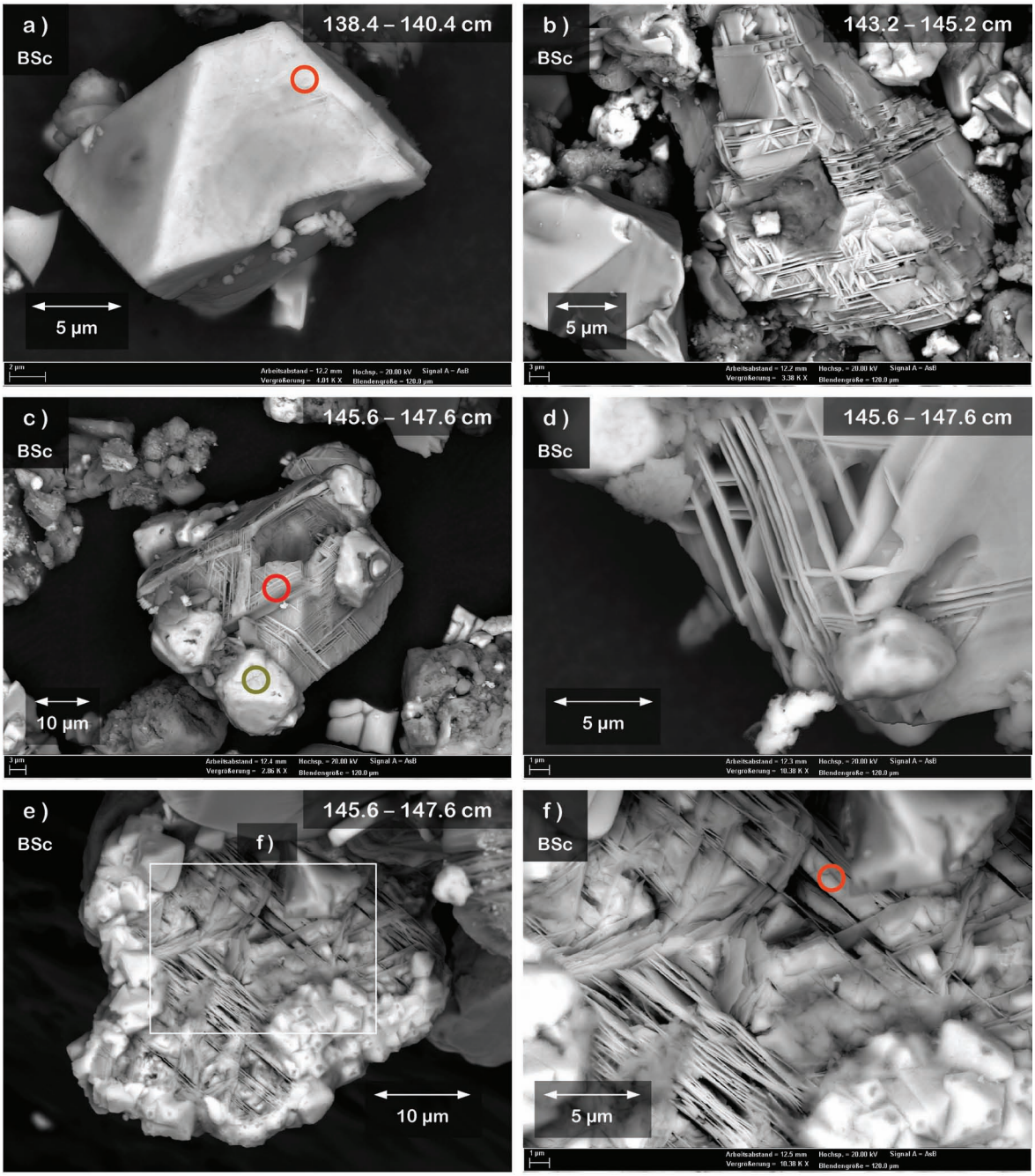
a)
BSc
138.4 – 140.4 cm
5 µm
b)
BSc
143.2 – 145.2 cm
5 µm
c)
BSc
145.6 – 147.6 cm
10 µm
d)
BSc
145.6 – 147.6 cm
5 µm
e)
BSc
f)
145.6 – 147.6 cm
10 µm
f)
BSc
5 µm

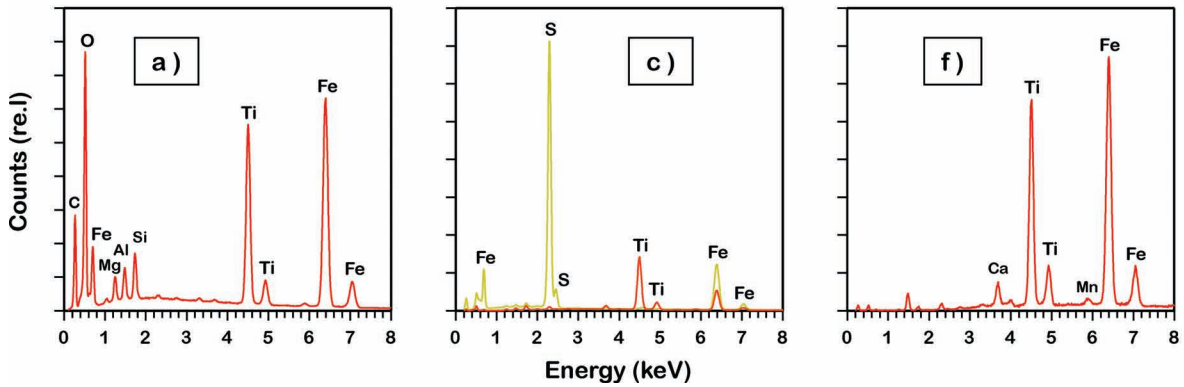
a)
O
C
Fe
Al
Mg
Si
Ti
Ti
Fe
Fe
c)
S
Fe
S
Ti
Ti
Fe
Fe
f)
Fe
Ti
Ca
Ti
Mn
Fe
Counts (re.l)
Energy (keV)
0 1 2 3 4 5 6 7 8

Plate 5

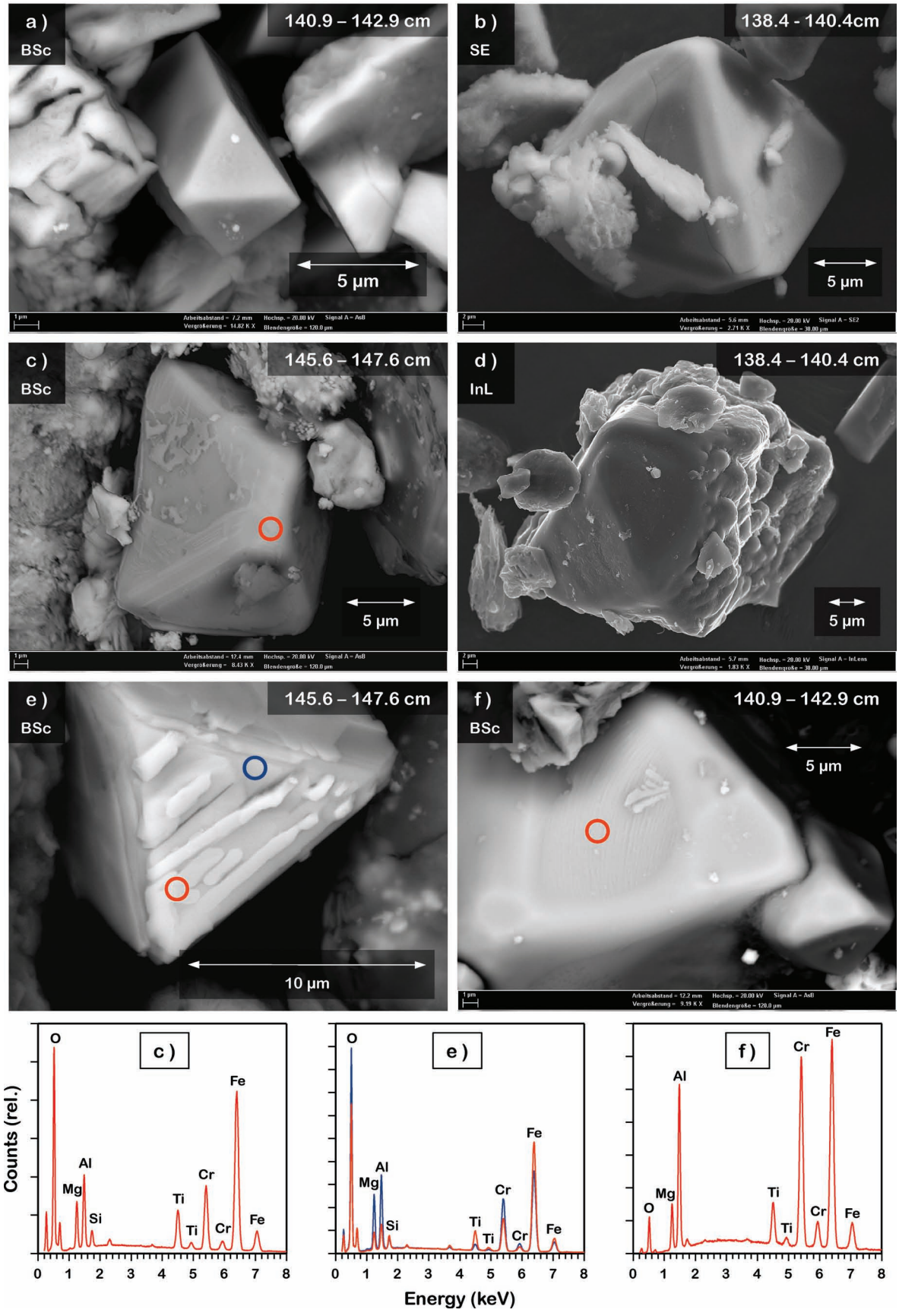
a)
BSc
140.9 – 142.9 cm
5 µm
b)
SE
138.4 - 140.4cm
5 µm
c)
BSc
145.6 – 147.6 cm
5 µm
d)
InL
138.4 – 140.4 cm
5 µm
e)
BSc
145.6 – 147.6 cm
10 µm
f)
BSc
140.9 – 142.9 cm
5 µm
c)
e)
f)
O
Mg
Al
Si
Ti
Cr
Fe
Counts (rel.)
Energy (keV)

Plate 6

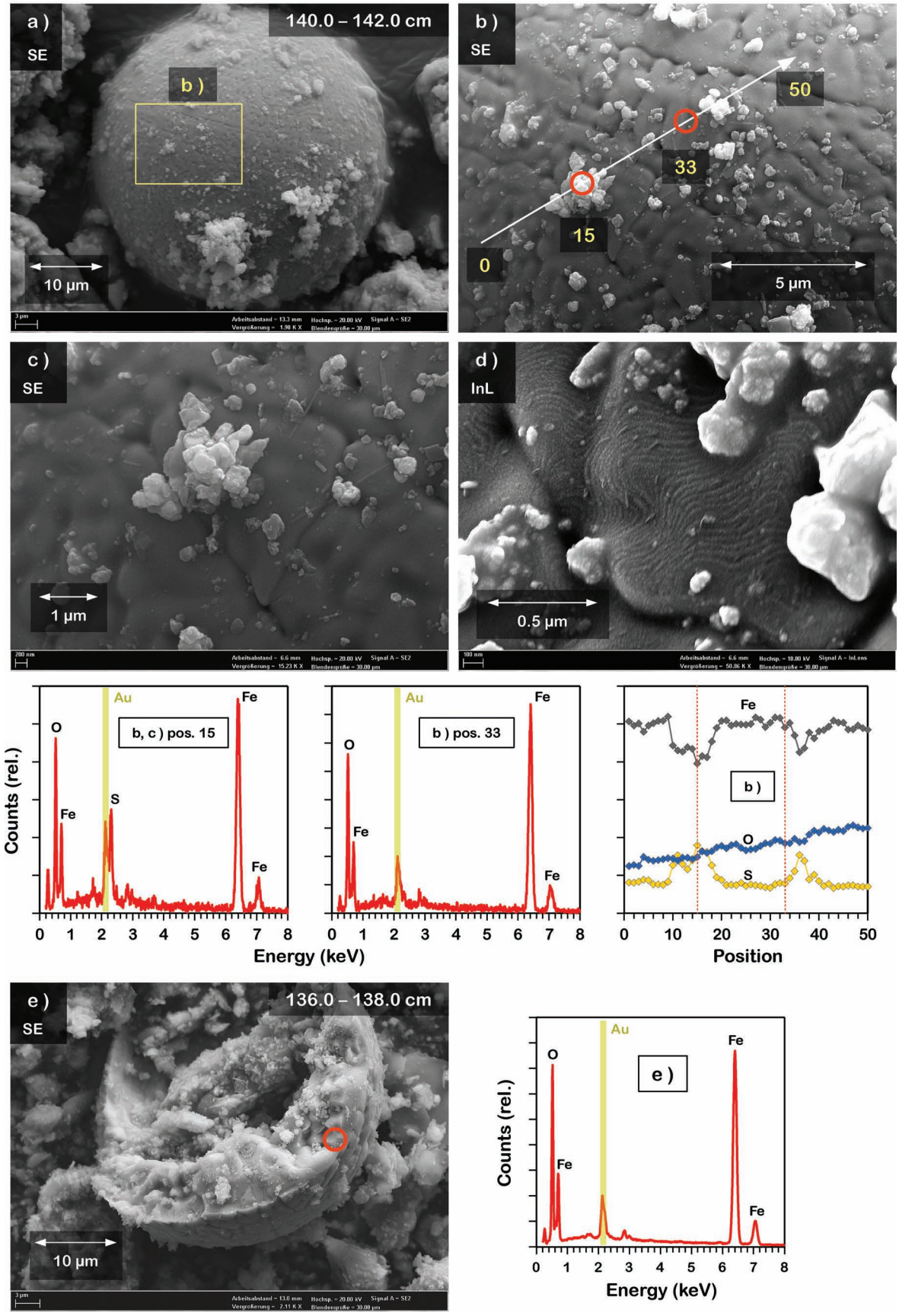
a)
SE
140.0 – 142.0 cm
b)
10 µm
b)
SE
50
33
15
0
5 µm
c)
SE
1 µm
d)
InL
0.5 µm
Au
O
Fe
S
b, c) pos. 15
Counts (rel.)
Energy (keV)
b) pos. 33
b)
Position
e)
SE
136.0 – 138.0 cm
10 µm
e)

Plate 7

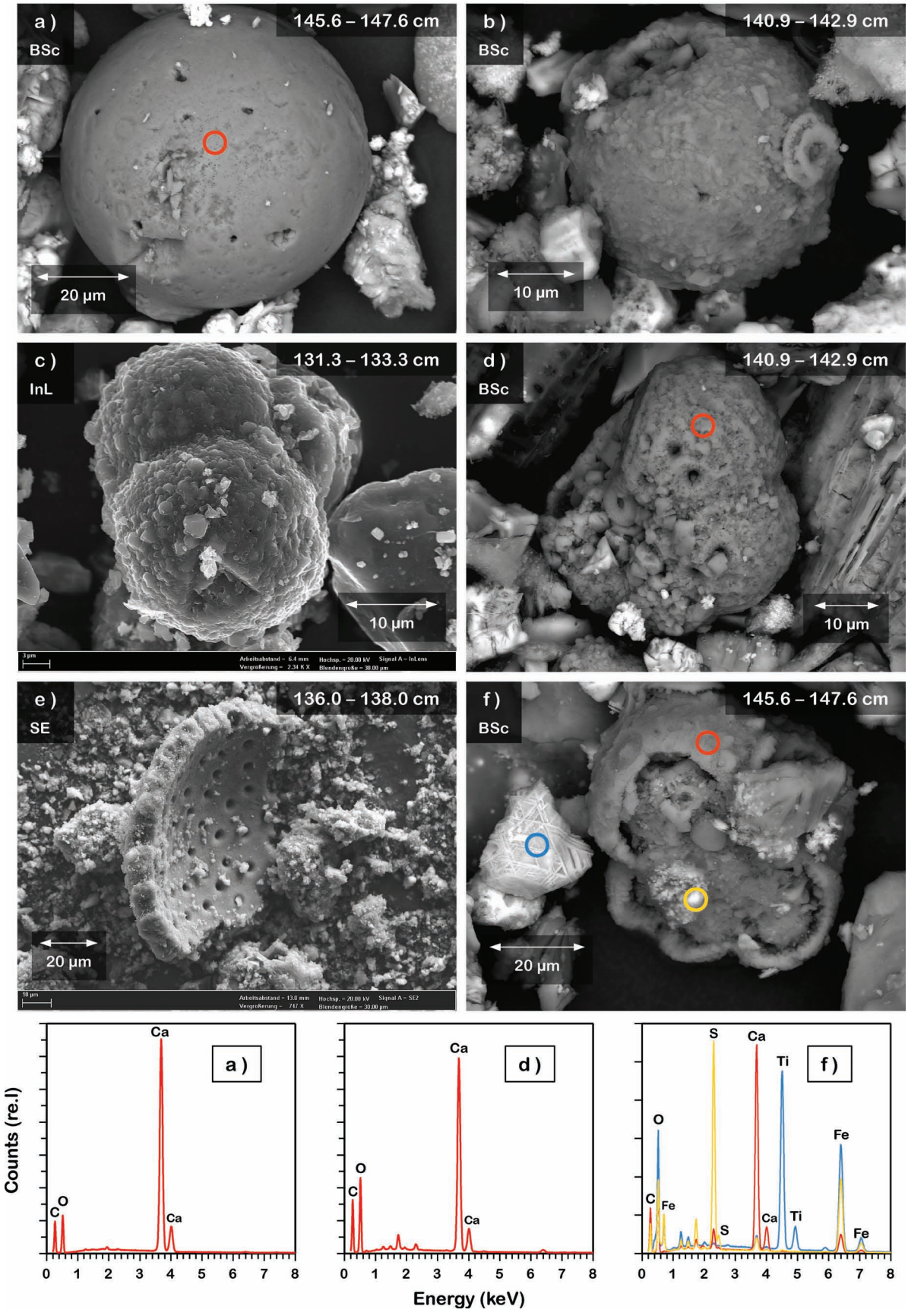
a)
BSc
145.6 – 147.6 cm
20 µm
b)
BSc
140.9 – 142.9 cm
10 µm
c)
InL
131.3 – 133.3 cm
10 µm
d)
BSc
140.9 – 142.9 cm
10 µm
e)
SE
136.0 – 138.0 cm
20 µm
f)
BSc
145.6 – 147.6 cm
20 µm
Counts (re.l)
Energy (keV)
a)
C
O
Ca
Ca
d)
C
O
Ca
Ca
f)
C
O
Fe
S
S
Ca
Ca
Ti
Ti
Fe
Fe
0 1 2 3 4 5 6 7 8

Plate 8

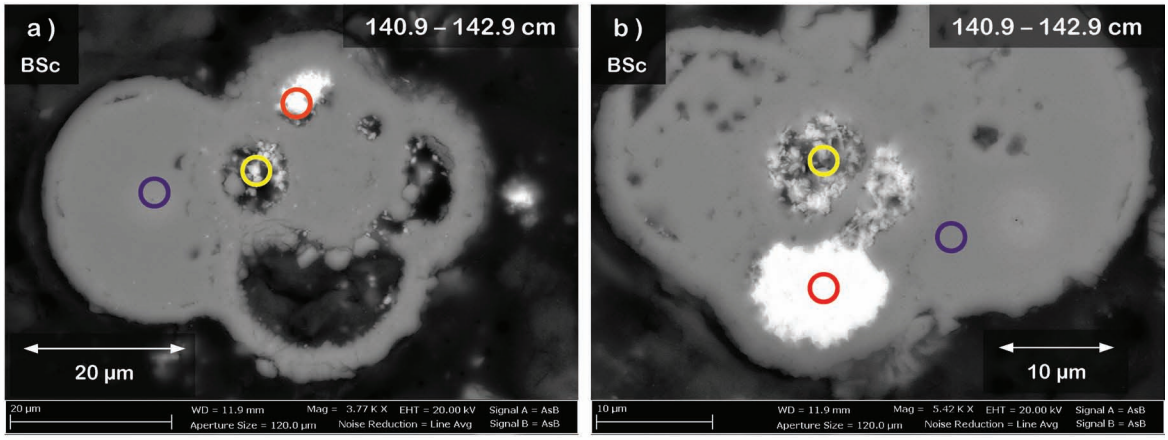
a)
BSc
140.9 – 142.9 cm
20 µm
b)
BSc
140.9 – 142.9 cm
10 µm

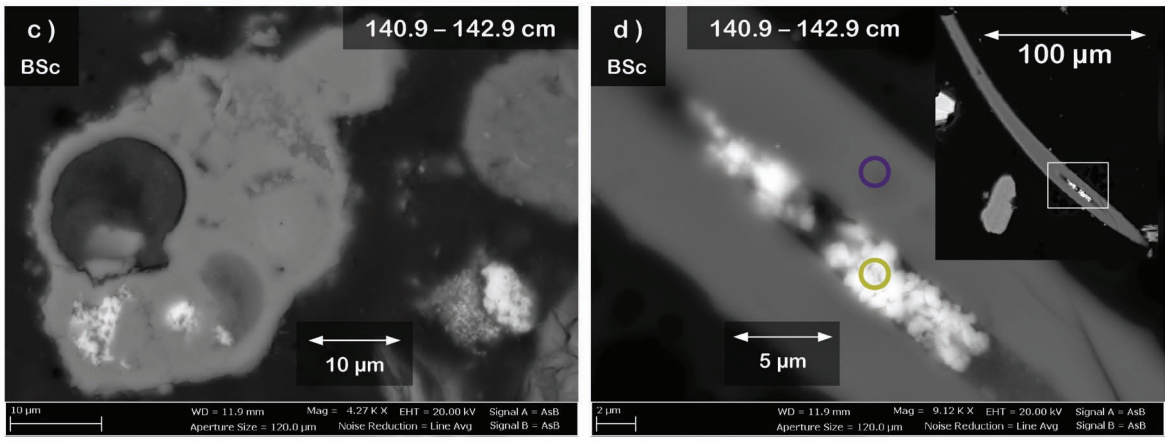
c)
BSc
140.9 – 142.9 cm
10 µm
d)
BSc
140.9 – 142.9 cm
100 µm
5 µm

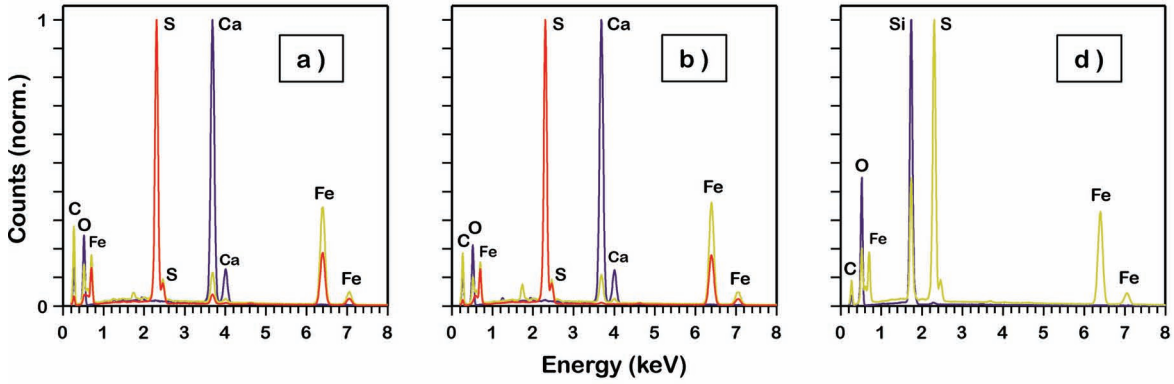
a)
b)
d)
Counts (norm.)
Energy (keV)
S
Ca
Si
C
O
Fe

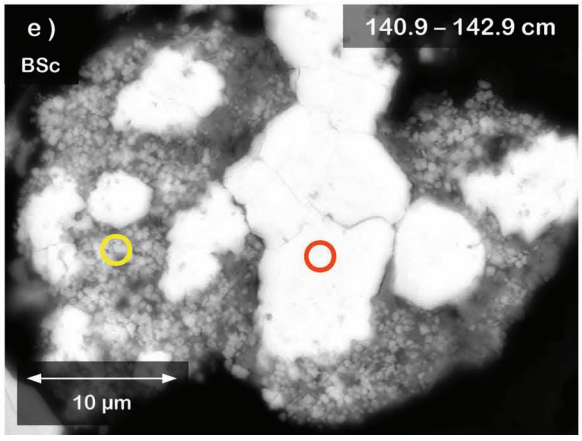
e)
BSc
140.9 – 142.9 cm
10 µm

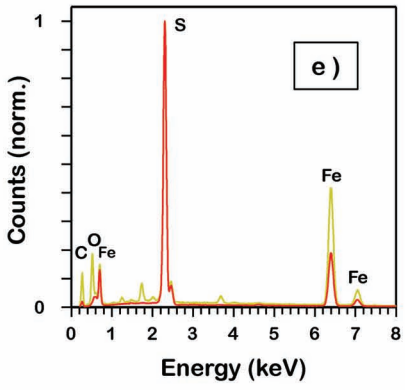
e)
Counts (norm.)
Energy (keV)
S
Fe
C
O

Plate 9

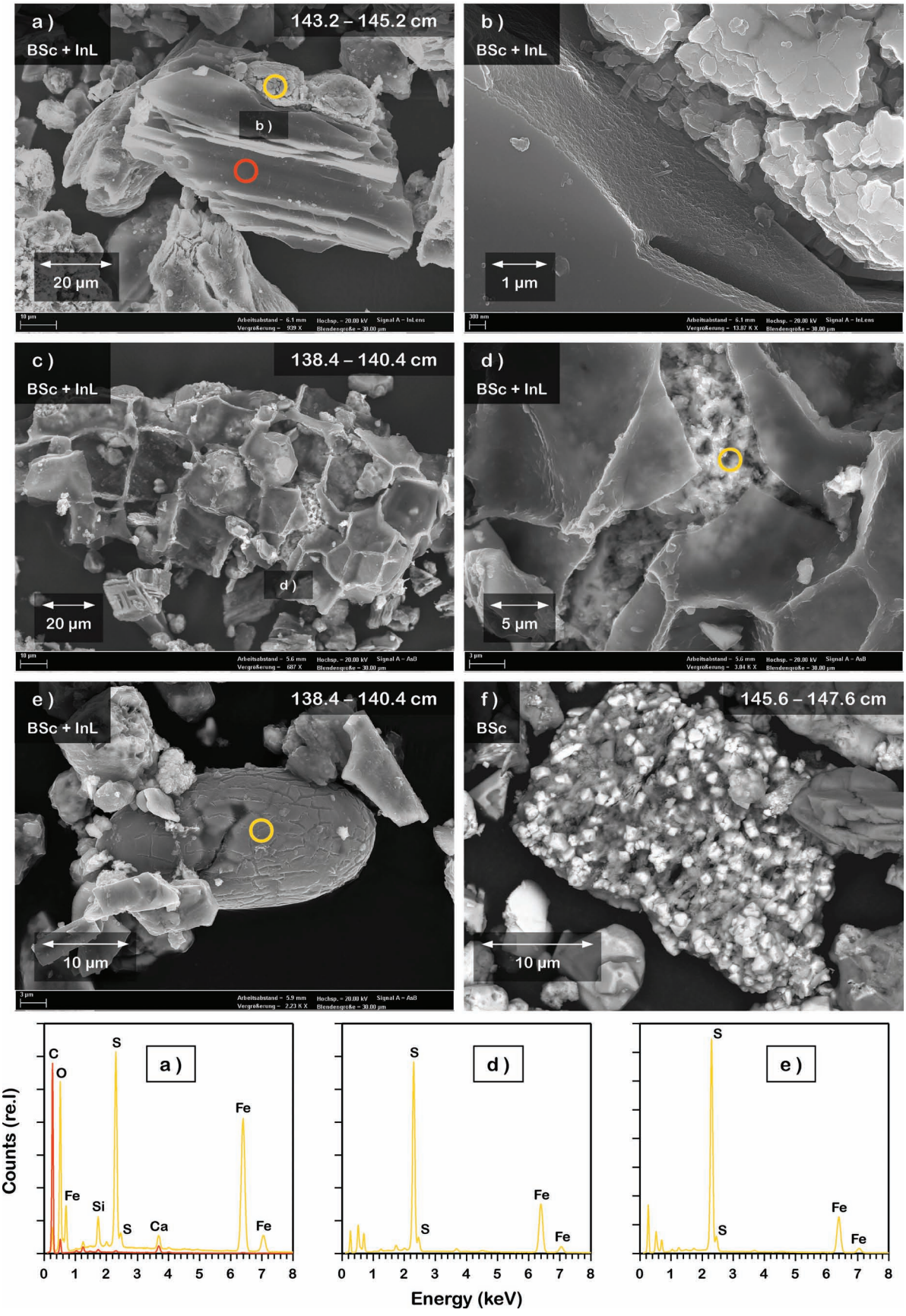
a)
BSc + InL
143.2 – 145.2 cm
b)
20 µm
b)
BSc + InL
1 µm
c)
BSc + InL
138.4 – 140.4 cm
d)
20 µm
d)
BSc + InL
5 µm
e)
BSc + InL
138.4 – 140.4 cm
10 µm
f)
BSc
145.6 – 147.6 cm
10 µm
a)
C
O
Fe
Si
S
S
Ca
Fe
Fe
d)
S
S
Fe
Fe
e)
S
S
Fe
Fe
Counts (re.l)
0 1 2 3 4 5 6 7 8
Energy (keV)

Plate 10

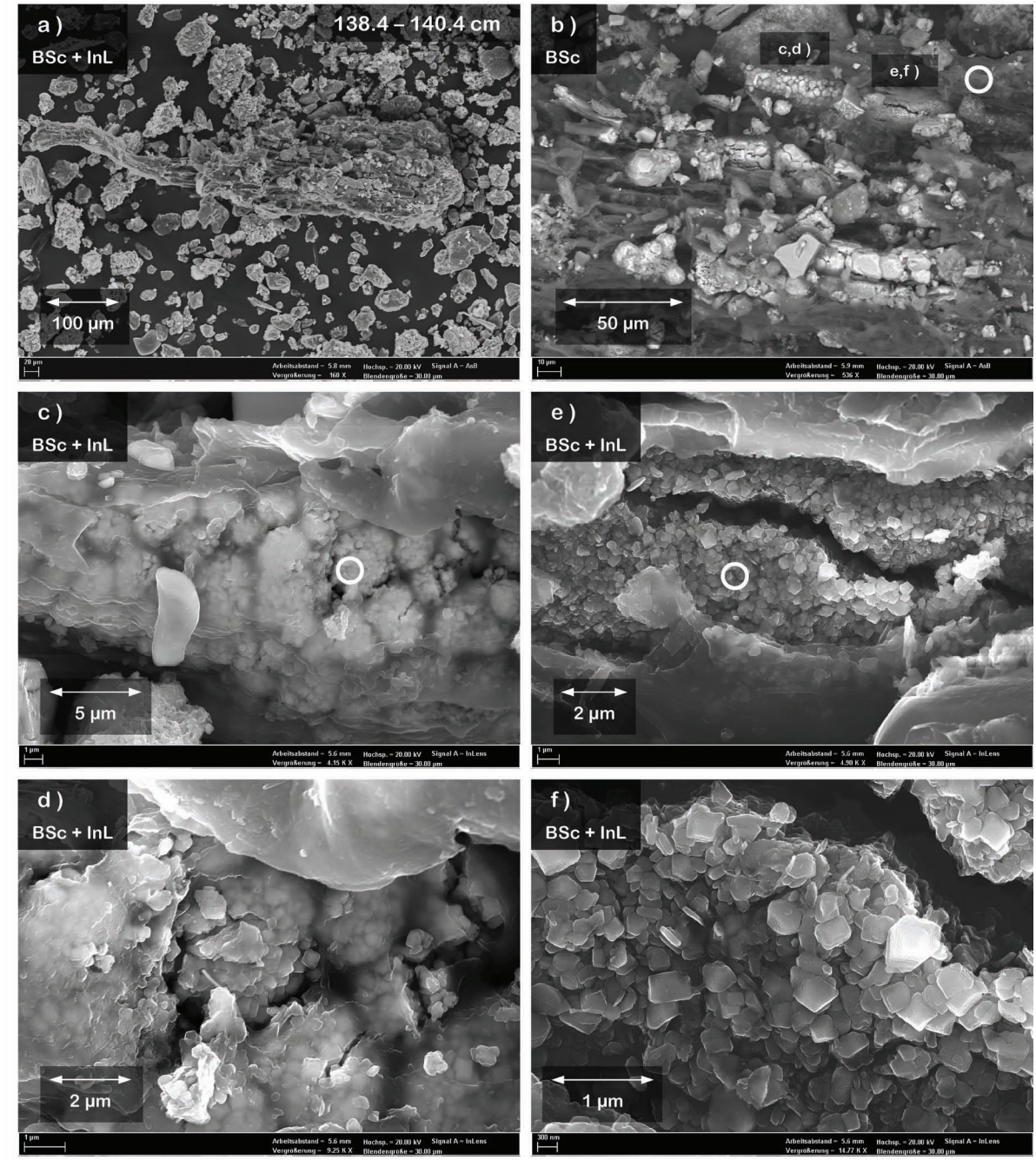
a)
BSc + InL
138.4 – 140.4 cm
100 µm
b)
BSc
c,d)
e,f)
50 µm
c)
BSc + InL
5 µm
e)
BSc + InL
2 µm
d)
BSc + InL
2 µm
f)
BSc + InL
1 µm

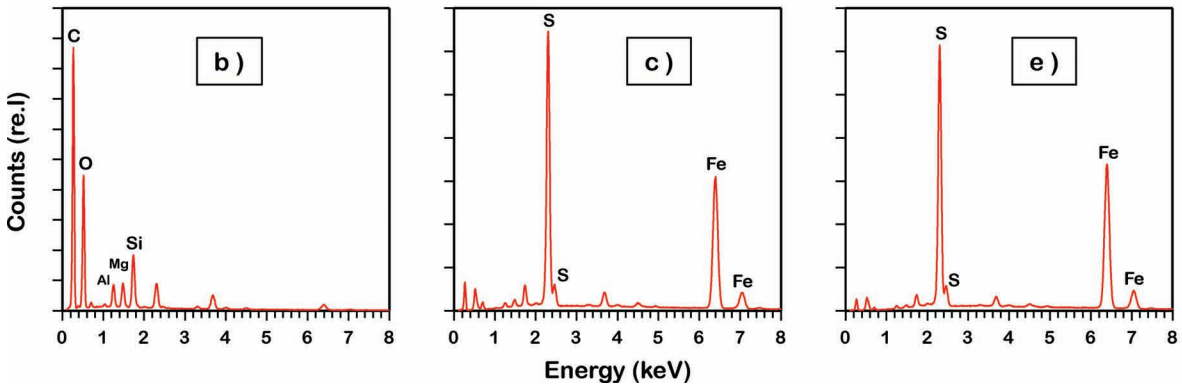
b)
c)
e)
C
O
Si
Mg
Al
S
Fe
Counts (re.l)
Energy (keV)
0 1 2 3 4 5 6 7 8

Plate 11

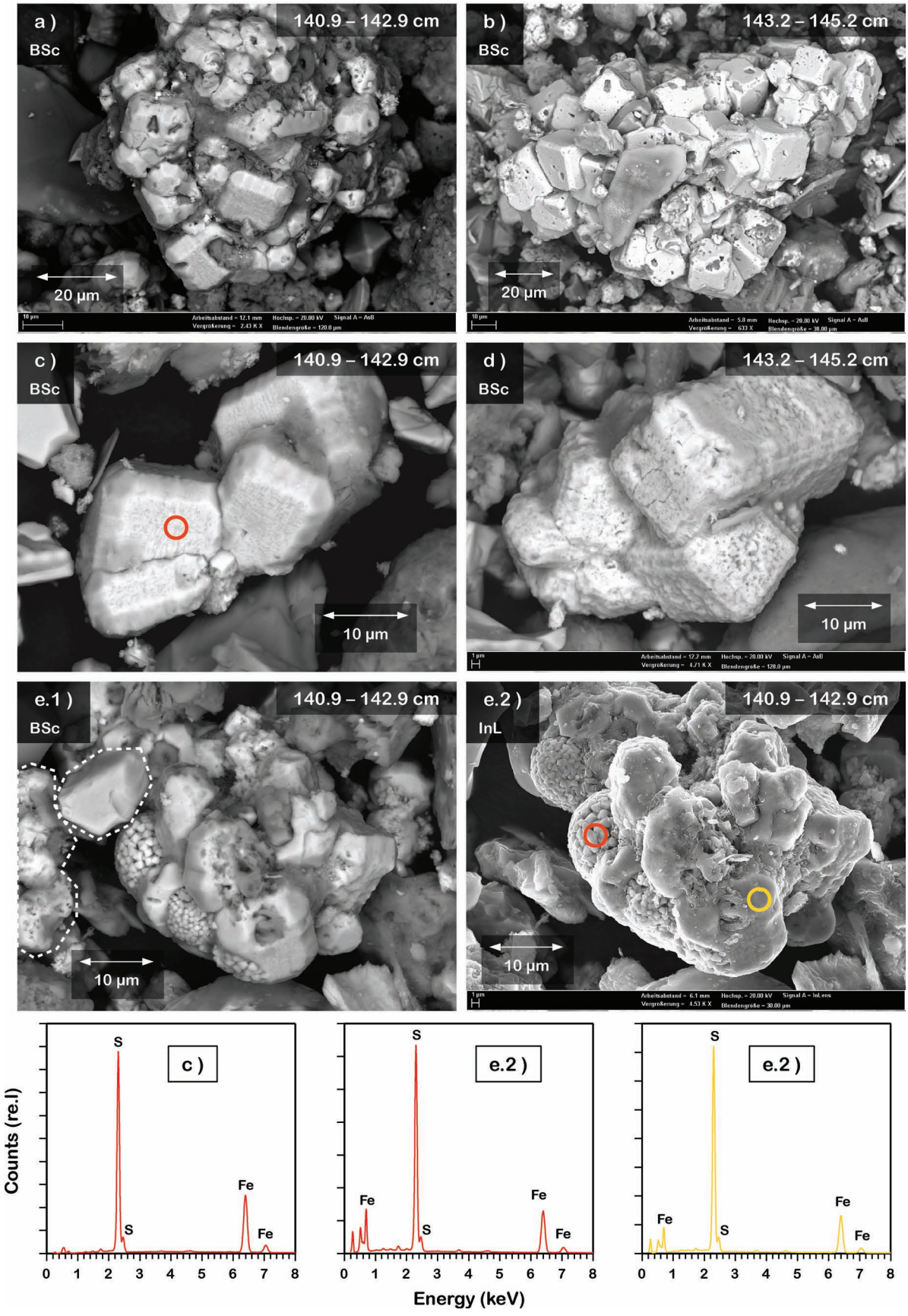
a)
BSc
140.9 – 142.9 cm
20 µm
b)
BSc
143.2 – 145.2 cm
20 µm
c)
BSc
140.9 – 142.9 cm
10 µm
d)
BSc
143.2 – 145.2 cm
10 µm
e.1)
BSc
140.9 – 142.9 cm
10 µm
e.2)
InL
140.9 – 142.9 cm
10 µm
c)
e.2)
e.2)
S
Fe
Counts (re.l)
Energy (keV)
0 1 2 3 4 5 6 7 8